

Photosphere emission from a hybrid relativistic outflow with arbitrary dimensionless entropy and magnetization in GRBs

He Gao, Bing Zhang

Department of Physics and Astronomy, University of Nevada Las Vegas, NV 89154, USA
gaohe@physics.unlv.edu; zhang@physics.unlv.edu

ABSTRACT

In view of the recent *Fermi* observations of GRB prompt emission spectra, we develop a theory of photosphere emission of a hybrid relativistic outflow with a hot fireball component (defined by dimensionless entropy η) and a cold Poynting-flux component (defined by magnetization σ_0 at the central engine). We consider the scenarios both without and with sub-photospheric magnetic dissipations. Based on a simplified toy model of jet dynamics, we develop two approaches: a “bottom-up” approach to predict the temperature (for a non-dissipative photosphere) and luminosity of the photosphere emission and its relative brightness for a given pair of (η, σ_0) ; and a “top-down” approach to diagnose central engine parameters (η and σ_0) based on the observed quasi-thermal photosphere emission properties. We show that a variety of observed GRB prompt emission spectra with different degrees of photosphere thermal emission can be reproduced by varying η and σ_0 within the non-dissipative photosphere scenario. In order to reproduce the observed spectra, the outflows of most GRBs need to have a significant σ , both at the central engine, and at the photosphere. The σ value at 10^{15} cm from the central engine (a possible non-thermal emission site) is usually also greater than unity, so that internal-collision-induced magnetic reconnection and turbulence (ICMART) may be the mechanism to power the non-thermal emission. We apply our top-down approach to GRB 110721A, and find that the temporal evolution behavior of its blackbody component can be well interpreted with a time-varying (η, σ_0) at the central engine, instead of invoking a varying engine base size r_0 as proposed by previous authors.

1. Introduction

After decades of investigations, the origin of gamma-ray burst (GRB) prompt emission is still poorly understood. The main obstacle in front of theorists is one fundamental question: *What is the composition of GRB jets?*

In the early picture discussed by Paczynski (1986) and Goodman (1986), GRB outflows originate from an initially hot “fireball” composed of photons and electron/positron pairs. The emergent spectrum from the fireball photosphere is a modified blackbody, which is inconsistent with the typical observed spectrum, characterized by a smoothly-joint broken power-law function known as the “Band” function (Band et al. 1993). Observationally, the typical low- and high-energy photon indices of the Band function are distributed around $\alpha \sim -1$ and $\beta \sim -2.2$, respectively (Preece et al. 2000), which disfavor a simplest fireball photosphere model. Shemi & Piran (1990) showed that when a small amount of baryons are added to the fireball, a significant fraction of the initial fireball thermal energy is converted to the kinetic energy of the outflow, after an initially rapid acceleration phase under fireball’s thermal pressure (Mészáros et al. 1993; Piran et al. 1993). In order to produce non-thermal photons, the kinetic energy of the outflow needs to be dissipated, either in the external shock (Rees & Mészáros 1992; Mészáros & Rees 1993) or internal shocks (hereafter IS, Rees & Mészáros 1994). Synchrotron (and possibly also synchrotron self-Compton) radiation by the relativistic electrons accelerated in these shocks give rise to the observed non-thermal γ -ray emission (Mészáros et al. 1994; Tavani 1996; Daigne & Mochkovitch 1998; Lloyd & Petrosian 2000). Within such a “fireball shock” model, the observed spectrum is expected to be the superposition of two components: a non-thermal component from the IS in the optically thin region, and a quasi-thermal component from the fireball photosphere (Mészáros & Rees 2000; Mészáros et al. 2002; Pe’er et al. 2006).

Before *Fermi*, it has been claimed that the spectra of some BATSE GRBs can be fit with the superposition of a blackbody component and an underlying power law (e.g. Ghirlanda et al. 2002, 2003; Ryde 2005; Ryde & Pe’er 2009). Due to the narrowness of the energy band, one was not able to exclude other models, so as to firmly establish the thermal model. Most BATSE GRBs, on the other hand, have a dominant Band function component for both time-integrated and time-resolved spectra. There are several competing models to interpret the peak energy E_p in the pre-*Fermi* era (Zhang & Mészáros 2002). If it is the synchrotron peak from the IS, then the absence of the photospheric emission component would imply that GRB jets are magnetically dominated (Daigne & Mochkovitch 2002; Zhang & Mészáros 2002). Within this scenario, the GRB radiation is powered by dissipation of the magnetic field energy in the ejecta (Usov 1994; Thompson 1994; Mészáros & Rees 1997; Lyutikov & Blandford 2003). Alternatively, the Band function itself may be emission from a dissipative photosphere (Rees & Mészáros 2005; Giannios 2008; Beloborodov 2010; Ioka 2010; Lazzati & Begelman 2010; Pe’er & Ryde 2011; Vurm et al. 2011; Giannios 2012; Lundman et al. 2013).

Having both Gamma-ray Burst Monitor (GBM, Meegan et al. 2009) and Large Area Telescope (LAT, Atwood et al. 2009) on board, *Fermi* opened the spectral window to cover

6-7 orders of magnitude in energy, allowing a close investigation of various spectral components in the GRB prompt emission spectra. The first bright LAT GRB, GRB 080916C, showed nearly featureless Band spectra in 5 different time bins over 6-7 orders of magnitude in energy (Abdo et al. 2009a; Zhang et al. 2011). Assuming the standard fireball shock model and using parameters derived from the observational data, Zhang & Pe’er (2009) showed that a quasi-thermal photosphere component would greatly outshine the non-thermal component if GRB 080916C is a fireball. The non-detection of such a bright photosphere component allowed Zhang & Pe’er (2009) to claim that the jet of GRB 080916C is Poynting-flux-dominated, and a lower limit of σ was set at the photosphere¹. In order to interpret the non-thermal emission in a Poynting flux dominated outflow, Zhang & Yan (2011) proposed an “internal-collision-induced magnetic reconnection and turbulence” (ICMART) model for GRBs.

The quasi-thermal component predicted by the fireball model was later observed in some *Fermi* GRBs. GRB 090902B (Abdo et al. 2009b) is the most prominent one, which shows a narrow Band function component superposed on an underlying power law component in the time integrated spectrum. When a time-resolved spectral analysis was carried out, a multi-color blackbody (Ryde et al. 2010) or even a blackbody (Zhang et al. 2011) component was revealed. This component is well interpreted as photosphere emission from a fireball (Pe’er et al. 2012). Later, several more GRBs have a thermal spectral component identified in the time-integrated and time-resolved spectra, but the component is sub-dominant (e.g. GRB 100724B, Guiriec et al. 2011; GRB 110721A, Axelsson et al. 2012; and the short GRB 120323A Guiriec et al. 2013). Since these thermal components are superposed on a Band component, it suggests that the Band emission component is not the modified thermal emission from the photosphere². Rather, the Band component likely originates from an optically thin region, e.g. the IS or the ICMART site. The fact that GRB 110721A has a 15-MeV E_p at early epochs disfavors a non-dissipative photospheric origin of the Band component, since it exceeds the maximum temperature a non-dissipative photosphere can reach for the observed luminosity (Zhang et al. 2012, see also Veres et al. 2012).

The available data suggest that the photosphere emission in GRBs has diverse proper-

¹A recent more detailed investigation (S. Guiriec et al. 2014, in preparation) revealed a weak photosphere component in GRB 080916C. Its peak flux is roughly at the flux level that Zhang & Pe’er (2009) used to derive the lower limit of σ . As a result, the conclusion of Zhang & Pe’er (2009) that GRB 080916C is a Poynting flux dominated remains valid, with the derived lower limit of σ replaced by the real value of σ .

²The photosphere model suffers from the difficulty to account for the low-energy photon index of the Band function, and may not account for the observed hard-to-soft E_p evolution pattern as observed in many GRBs (Deng & Zhang 2014).

ties. While in rare cases (e.g. GRB 090902B) it can be the dominant emission component, in many more cases, it is either a sub-dominant component, or non-detectable. A plausible interpretation (e.g. Zhang 2011) would be that GRBs have a diverse jet composition. While some are more matter-dominated (which resemble traditional fireballs), many others have more magnetized ejecta with a range of magnetization degree (σ) at the central engine, the photosphere, and the non-thermal emission site. Two key parameters are the dimensionless entropy η and magnetization σ_0 at the central engine. If η is large and $\sigma_0 \ll 1$, one gets a hot fireball with a dominant photosphere component (e.g. in GRB 090902B). If η is smaller while σ_0 is larger, the thermal emission is suppressed, so that the photosphere emission component is sub-dominant (e.g. in GRB 110721A). Finally, if η is close to unity while σ_0 is extremely large, the photosphere component is completely suppressed. This is an attractive possibility. However, so far no theory of photosphere emission of such a hybrid outflow has been developed in detail.

Within the framework of the fireball shock model, Pe’er et al. (2007) proposed a method to infer central engine parameters using observed data. With the measured temperature and flux of an identified thermal component in the spectrum, along with a flux ratio between thermal and non-thermal components, one may infer the size of the jet at the base of the outflow, r_0 , and the dimensionless entropy of the outflow, $\eta = L_w/\dot{M}c^2$ (which is also the bulk Lorentz factor of the outflow, if the photosphere radius is greater than the fireball coasting radius). Some authors have applied this method to some *Fermi* GRBs (Iyyani et al. 2013; Preece et al. 2014; Ghirlanda et al. 2013). The derived central engine parameters are sometimes ad hoc or inconsistent. For instance, the analyses for GRB 110721A (Iyyani et al. 2013) and for GRB 130427A (Preece et al. 2014) led to a curious conclusion that the bulk Lorentz factor of the outflow of different layers are decreasing with time. This would lead to no, or at most very inefficient, internal shock emission. Yet both bursts have dominant non-thermal emission. More curiously, the data of GRB 110721A (Iyyani et al. 2013) require that r_0 is rapidly varying with time by 2-3 orders of magnitudes. This is hard to imagine given the well believed paradigm of GRB central engine: If the engine is naked, the size of the engine (a hyper-accreting black hole or a millisecond magnetar) is around $r_0 \sim 10^7$ cm; if an extended envelope of a collapsar progenitor is considered, the fireball may be “re-born”, with $r_0 \sim R_*\theta_j \sim 10^9 R_{*,10}\theta_{j,-1}$ cm (where R_* is the size of the progenitor star, and θ_j is the jet opening angle). If one considers the depletion of the envelope, r_0 should decrease with time. However, Iyyani et al. (2013) showed that r_0 increases from 10^6 cm to 10^8 cm early on, and then decreases mildly after 2 seconds. These absurd conclusions suggest that the starting point of the analysis, i.e. the assumption of a pure fireball model, might not be valid. It is interesting to see whether a hybrid ejecta photosphere model may solve the problem. Incidentally, Ghirlanda et al. (2013) analyzed another burst GRB 100507 using

the fireball framework (Pe’er et al. 2007), but found that the derived r_0 remains constant and reasonable. The jet composition of that burst may be more close to a fireball. It would be interesting to see whether a general theoretical framework can be established, which may be reduced to the standard fireball framework when $\sigma_0 < 1$.

In this paper, we develop a theory of photosphere emission from a hybrid relativistic outflow with an arbitrary dimensionless entropy η and magnetization σ_0 at the central engine based on a simplified toy model of the dynamical evolution of a hybrid jet. In section 2, we describe the set-up of the problem, and introduce an approximate analytical description of the dynamical evolution of the hybrid system. In section 3, we develop a “bottom-up” approach by deriving the photosphere properties for given input parameters of the central engine. We then reverse the problem and develop a “top-down” approach in section 4, aiming at diagnosing the central engine parameters based on the observational data of the thermal emission component as well as its relative brightness with respect to the non-thermal component. In section 5, we apply this method to GRB 110721A and derive its central engine parameters as well as their temporal evolution. Throughout the paper, the convention $Q = 10^n Q_n$ is adopted for cgs units.

2. Hybrid system and its dynamical evolution

The acceleration of a GRB jet may be proceeded with two mechanisms: thermally driven or magnetically driven. The former is relevant for a hot fireball, which proceeds very rapidly; whereas the latter is relevant for a Poynting flux dominated outflow, which proceeds relatively more slowly. In realistic central engine models invoking either a hyper-accreting black hole or a rapidly spinning magnetar, the central engine very likely carries two components: a “hot” component due to neutrino heating from the accretion disk or the proto neutron star, and a “cold” component related to a Poynting flux launched from the black hole or the neutron star (e.g. Lei et al. 2013; Metzger et al. 2011). The central engine may be characterized by a parameter

$$\mu_0 = \frac{L_w}{\dot{M}c^2} = \frac{L_{h,0} + L_{c,0}}{\dot{M}c^2} = \eta(1 + \sigma_0), \quad (1)$$

which defines the total energy per baryon at the central engine, where $L_{h,0} = \eta\dot{M}c^2$, $L_{c,0} = L_{P,0}$, and L_w are the luminosities of the hot component, cold (Poynting flux) component, and the entire wind, respectively. The dimensionless entropy η defines average total energy (rest mass energy plus thermal energy) per baryon in the hot component, and the magnetization

parameter σ_0 is defined as³

$$\sigma_0 \equiv \frac{L_c}{L_h} = \frac{L_P}{\eta \dot{M} c^2}. \quad (2)$$

For a variable central engine, all the parameters are a function of t . For each slice of wind materials (launched within a short time interval), all the parameters are a function of r , the radius from the central engine.

Regardless of how the parameters evolve with the radius r , at any distance, one may define a parameter (Zhang 2014)

$$\mu(r) = \Gamma(r)\Theta(r)(1 + \sigma(r)), \quad (3)$$

where Γ is the bulk Lorentz factor, Θ is the total co-moving energy per baryon ($\Theta - 1$ is the thermal energy), and σ is the ratio between comoving cold (magnetic) and hot (matter) energy densities. All the parameters are a function of r , and should evolve with r . If no additional baryon loading occurs and if there is no energy loss in the system, one has a conserved μ value

$$\mu = \Gamma\Theta(1 + \sigma) = \eta(1 + \sigma_0) = \mu_0 = \text{const.} \quad (4)$$

In reality, leakage of radiation energy (the GRB emission itself) is inevitable, so that one should have $\mu < \mu_0$.

The dynamical evolution (the evolution of $\Gamma(r)$ and $\sigma(r)$) of a hybrid system is not studied in detail. The jet dynamics in the two extreme cases, however, are well studied.

For $\eta \gg 1$ and $\sigma_0 \ll 1$ (a pure fireball), Γ would firstly increase linearly with r until reaching the maximum Lorentz factor defined by η (or a characteristic value η_c if $\eta > \eta_c$, Mészáros & Rees 2000), then “coasts” at the maximum value until the IS radius, where fast shells catch up with slow shells and dissipate kinetic energy through shocks. After the IS phase, the average Lorentz factor of the flow decreases, since a significant amount of energy is lost in the form of radiation. The ejecta keeps coasting (probably with minor decrease of Lorentz factor due to residue ISs, e.g. Li & Waxman 2008) until reaching the deceleration radius beyond which the inertia from the circumburst medium is large enough and the Lorentz factor of the blastwave decreases as a power law with radius (e.g. $\Gamma \propto r^{-3/2}$ for a constant density medium).

For $\eta \sim 1$ and $\sigma_0 \gg 1$ (a Poynting flux dominated outflow), the jet dynamics is more complicated. Generally, the flow can be quickly accelerated to a “magneto-sonic point”,

³The traditional definition of σ is the ratio between the Poynting flux and the kinetic flux of matter. For the hybrid system studied this paper, it is more convenient to also include internal energy in the matter flux in the definition of a more generalized σ .

beyond which the jet front loses causal contact from the engine. For a cold Poynting flux dominated outflow, the fast magnetosonic speed is essentially the Alfven speed. For a high- σ flow, the “Alfvenic” Lorentz factor is

$$\Gamma_A = (1 + \sigma)^{1/2}. \quad (5)$$

The magnetosonic point, which we call the radius of rapid acceleration r_{ra} in the rest of the paper, is defined when the bulk Lorentz factor equals the “Alfvenic” Lorentz factor, so that (Li et al. 1992; Komissarov et al. 2009; Kumar & Zhang 2015)

$$\Gamma_{\text{ra}} = (1 + \sigma_0)^{1/3} \simeq \sigma_0^{1/3} \quad (6)$$

and

$$(1 + \sigma_{\text{ra}}) = (1 + \sigma_0)^{2/3}, \quad (7)$$

or $\sigma_{\text{ra}} \simeq \sigma_0^{2/3}$. Here $\Gamma_{\text{ra}} = \Gamma(r_{\text{ra}})$ and $\sigma_{\text{ra}} = \sigma(r_{\text{ra}})$ are the Lorentz factor and σ value at r_{ra} , respectively. The acceleration law during this rapid acceleration phase may be written as a power law, $\Gamma \propto r^\lambda$, with the power-law index λ defined by the geometric configuration of the GRB jet. The value of λ may be between 1/2 and 1 (e.g. Komissarov et al. 2009; Granot et al. 2011). Since the exact value does not affect the main conclusion of this work, for simplicity, we adopt $\lambda = 1$ in the rest of the discussion, so that this acceleration phase can be treated as similar to the thermally-driven case. The caveat of this assumption will be discussed in detail in section 6.

Above r_{ra} , since σ is still $\gg 1$, continued acceleration of the ejecta is still possible. However, the acceleration is slow and delicate, depending on the detailed magnetic configuration, and whether there is significant magnetic dissipation along the way. The most rapid acceleration would have a power law form $\Gamma \propto r^{1/3}$, either due to continuous magnetic dissipation (Drenkhahn & Spruit 2002) or via an impulsive acceleration mechanism (Granot et al. 2011). In general, such a process may be described by a general acceleration law $\Gamma \propto r^\delta$ with $0 < \delta \leq 1/3$ (e.g. Mészáros & Rees 2011; Veres & Mészáros 2012). Ideally, the acceleration would continue until reaching the coasting radius r_c where Γ reaches σ_0 . However, if σ_0 is large enough, the jet may start to decelerate before the maximum Γ is reached ($r_{\text{dec}} < r_c$, e.g. Granot 2012). Furthermore, due to the internal irregularity of the outflow, multiple internal collisions within the moderately high- σ jet would trigger ICMART events to dissipate magnetic energy (Zhang & Yan 2011). This would lead to a sudden drop of σ and an abrupt increase of Γ in the emission region (e.g. Zhang & Zhang 2014). If the ejecta are individual magnetic blobs (e.g. Yuan & Zhang 2012), magnetic dissipation is facilitated since one collision would trigger significant reconnection activities, as verified by numerical simulations (W. Deng et al. 2015, in preparation).

When a Poynting flux propagates inside a star, the jet may be collimated by the stellar envelope. The confinement may lead to an additional magnetic acceleration once the jet exits the star (Tchekhovskoy et al. 2009). Such an acceleration critically depend on the collimation profile inside the stellar envelope. Tchekhovskoy et al. (2009) assumed $\theta(r) \propto r^{-\nu/2}$ so that the confine pressure is a power law function of radius $p \propto r^{-\alpha}$, with $\alpha = 2(2 - \nu)$. In their simulation, they specifically adopted $\nu = 3/4$ so that $p \propto r^{-5/2}$. The reason to adopt this value is that it is consistent with the profile of a jet-shocked stellar envelope during the propagation of a relativistic jet inside a star (e.g. Zhang et al. 2003). As a result, the additional acceleration phase depicted by Tchekhovskoy et al. (2009) would be relevant for the very early episode of jet emission when it first breaks out the envelope. During the majority of the jet emission phase, a continuous jet launched from the central engine would pass freely through the already opened envelope. We speculate that the extra confinement effect discussed by Tchekhovskoy et al. (2009) would not play an essential role, and therefore ignore this effect in the treatment below. Nonetheless, we caution that the results would be affected if this collimation factor turns out to be important.

For a more complicated hybrid jet system, we make the assumption that acceleration proceeds first thermally and then magnetically (e.g. Mészáros & Rees 1997; Vlahakis & Königl 2003). Since thermal acceleration proceeds linearly, and the early magnetic acceleration below the magneto-sonic point also proceeds rapidly, we approximately assume that the ejecta first gets accelerated with $\Gamma \propto r$ until reaching a more generally defined *rapid acceleration* radius r_{ra} defined by the larger one of the thermal coasting radius and the magneto-sonic point. Even though magnetic acceleration may deviate from the linear law below r_{ra} , the mix with thermal acceleration would make the acceleration law in this phase very close to linear.

There are two situations. If $\eta > (1 + \sigma_0)^{1/2}$, after the linear acceleration phase of a fireball, the Lorentz factor of the magnetized outflow already exceeds its Alfven Lorentz factor, so that no rapid acceleration can be proceeded magnetically. One therefore has, for $\eta > (1 + \sigma_0)^{1/2}$,

$$\begin{aligned} \Gamma_{\text{ra}} &= \frac{\eta}{\Theta_{\text{ra}}}, \\ 1 + \sigma_{\text{ra}} &= 1 + \sigma_0. \end{aligned} \tag{8}$$

Notice that σ essentially does not decrease during this phase, but the matter portion of the luminosity changes from the thermal form to the kinetic form.

In the opposite regime, i.e. $\eta < (1 + \sigma_0)^{1/2}$, after the thermal acceleration phase, the outflow still moves with a Lorentz factor smaller than Γ_A (Eq.(2)), so that it can still undergo

rapid acceleration until $\Gamma_{\text{ra}} = \Gamma_A$ is satisfied. One therefore has, for $\eta < (1 + \sigma_0)^{1/2}$,

$$\begin{aligned}\Gamma_{\text{ra}} &= \left[\frac{\eta}{\Theta_{\text{ra}}} (1 + \sigma_0) \right]^{1/3}, \\ 1 + \sigma_{\text{ra}} &= \left[\frac{\eta}{\Theta_{\text{ra}}} (1 + \sigma_0) \right]^{2/3}.\end{aligned}\tag{9}$$

Putting these together, one can generally define

$$\Gamma_{\text{ra}} = \max \left(\frac{\eta}{\Theta_{\text{ra}}}, \left[\frac{\eta}{\Theta_{\text{ra}}} (1 + \sigma_0) \right]^{1/3} \right),\tag{10}$$

and

$$1 + \sigma_{\text{ra}} = \min \left(1 + \sigma_0, \left[\frac{\eta}{\Theta_{\text{ra}}} (1 + \sigma_0) \right]^{2/3} \right).\tag{11}$$

Here $\Theta_{\text{ra}} \sim 1$ is the total co-moving energy per baryon at r_{ra} .

Beyond r_{ra} , the jet would undergo a relatively slow acceleration with $\Gamma \propto r^\delta$ until reaching a *coasting radius* r_c . If one ignores radiation energy loss, the coasting Lorentz factor would be

$$\Gamma_c = \frac{\eta(1 + \sigma_0)}{\Theta_c(1 + \sigma_c)} \simeq \eta(1 + \sigma_0),\tag{12}$$

since $\Theta_c \sim 1$, and $\sigma_c \ll 1$. Here Γ_c , σ_c , and Θ_c are the Lorentz factor, magnetization parameter, and comoving energy per baryon at r_c , respectively.

In summary, if one ignores deceleration and energy loss, the Γ evolution for a hybrid system may be approximated as

$$\Gamma(r) = \begin{cases} \frac{r}{r_0}, & r_0 < r < r_{\text{ra}}; \\ \Gamma_{\text{ra}} \left(\frac{r}{r_{\text{ra}}} \right)^\delta, & r_{\text{ra}} < r < r_c; \\ \Gamma_c, & r > r_c, \end{cases}\tag{13}$$

where r_0 is the radius of the jet base (size of the central engine), $r_{\text{ra}} = \Gamma_{\text{ra}} r_0$, Γ_{ra} follows eq.(10),

$$r_c = r_{\text{ra}} \left(\frac{\Gamma_c}{\Gamma_{\text{ra}}} \right)^{1/\delta},\tag{14}$$

and Γ_c follows Eq.(12).

In reality, one has to consider jet deceleration at a radius r_{dec} , as well as possible internal energy dissipation and radiation loss at the IS radius, r_{IS} (if dissipation occurs during the

coasting phase), or at the ICMART radius, r_{ICMART} (if dissipation happens during the slow acceleration phase where σ is still > 1). Which situation occurs depends on the initial condition (η, σ_0) . In Figure 1, we present the evolution of Γ and σ with respect to the radius r for different input parameters. We assume the ICMART radius (r_{ICMART}) and IS radius (r_{IS}) are both at 10^{15} cm, with radius defined as r_{IS} if it is in the coasting phase, but as r_{ICMART} if it is in the slow acceleration phase. If $\sigma(r_{15}) > 1$, ICMART events would occur, which would increase Γ and reduce σ dramatically (Zhang & Yan 2011). The deceleration radius r_{dec} here is defined as the radius where the total energy of the swept-up matter from the interstellar medium (ISM) is half of the kinetic energy of the jet. We assume $E_K = 10^{52}$ erg and the number density of ISM $n = 1 \text{ cm}^{-3}$ to calculate r_{dec} . The results suggest that unless σ_0 is relatively small (say, below 80 for $\eta = 10$), the energy dissipation region (non-thermal emission region) is generally in the slow acceleration phase where $\sigma > 1$, so that ICMART rather than IS would be the main mechanism to power the observed non-thermal emission from GRBs. This point is also obvious in view that for typical parameters, the value of the derived r_c is typically $> 10^{15}$ cm.

3. Photosphere emission from a hybrid jet: the bottom-up approach

The photosphere radius, r_{ph} , is defined by the condition that the photon optical depth for Thomson scattering drops below unity, so that photons previously trapped in the fireball can escape. In the lab frame, this condition is written as

$$\tau = \int_{r_{\text{ph}}}^{\infty} n_e \sigma_T ds = 1, \quad (15)$$

where σ_T is the Thomson cross section, the lab frame electron number density can be written as

$$n_e = \frac{L_w \mathcal{V}}{4\pi r^2 m_p c^3 \eta (1 + \sigma_0)}, \quad (16)$$

and

$$ds = (1 - \beta \cos \theta) dr / \cos \theta \quad (17)$$

is the spatial increment in the outflow wind in the lab frame (e.g. Eq.(23) of Deng & Zhang 2014), θ is the angle from line-of-sight, m_p is proton mass, c is speed of light, and \mathcal{V} is the lepton-to-baryon number ratio. We assume that $\mathcal{V} \ll m_p/m_e$ is satisfied, so that the inertia of the leptons is negligible. Consider the line of sight direction ($\theta = 0$), one has $ds = (1 - \beta)dr \simeq dr/(2\Gamma^2)$. For Γ evolution as shown in Equation (13), the line-of-sight

photosphere radius can be derived as

$$r_{\text{ph}} = \begin{cases} \left(\frac{L_w \mathcal{V} \sigma_{\text{T}} r_0^2}{8\pi m_p c^3 \eta (1+\sigma_0)} \right)^{1/3}, & r_0 < r_{\text{ph}} < r_{\text{ra}}; \\ \left(\frac{L_w \mathcal{V} \sigma_{\text{T}} r_{\text{ra}}^{2\delta}}{8\pi m_p c^3 \Gamma_{\text{ra}}^2 \eta (1+\sigma_0)} \right)^{1/(2\delta+1)}, & r_{\text{ra}} < r_{\text{ph}} < r_{\text{c}}; \\ \frac{L_w \mathcal{V} \sigma_{\text{T}}}{8\pi m_p c^3 \Gamma_{\text{c}}^2 \eta (1+\sigma_0)}, & r_{\text{ph}} > r_{\text{c}}. \end{cases} \quad (18)$$

As shown in Pe’er et al. (2007), for quasi-thermal photosphere emission as expected in a non-dissipative photosphere, the observed temperature and thermal flux can be derived as

$$T_{\text{ob}} = C_1 \Gamma_{\text{ph}} T'_{\text{ph}} / (1+z), \quad (19)$$

$$F_{\text{BB}} = \mathcal{R}^2 \sigma_{\text{SB}} T_{\text{ob}}^4, \quad (20)$$

where

$$\mathcal{R} = C_2 \frac{(1+z)^2}{d_L} \frac{r_{\text{ph}}}{\Gamma_{\text{ph}}}, \quad (21)$$

z is the redshift, d_L is the luminosity distance, σ_{SB} is the Stefan-Boltzmann constant, T'_{ph} is the comoving temperature at the photosphere radius r_{ph} , and $C_1 \simeq 1.48$ and $C_2 \simeq 1.06$ are the factors derived from detailed numerical integration of angle- and distance-dependent photosphere emission.

The photosphere properties depends on whether significant magnetic energy dissipation happens below the photosphere radius r_{ph} . This is an open question, and no firm conclusion has been drawn from the first principles. In the following, we discuss both scenarios.

3.1. The case of no magnetic dissipation

This scenario assumes that no magnetic field reconnection occurs below the photosphere, so that no magnetic energy is directly converted to particle energy and heat. Magnetic acceleration in any case proceeds, so that some magnetic energy is converted to the kinetic energy of the outflow. Such a scenario may be relevant to helical jets or self-sustained magnetic bubbles (e.g. Spruit et al. 2001; Uzdensky & MacFadyen 2006; Yuan & Zhang 2012). This scenario predicts a quasi-thermal photosphere emission component, which is consistent with the data of several Fermi GRBs (e.g. Ryde et al. 2010; Zhang et al. 2011; Guiriec et al. 2011; Axelsson et al. 2012; Guiriec et al. 2013).

Without magnetic heating, the thermal energy undergoes adiabatic cooling, with $r^2 e^{3/4} \Gamma = \text{const}$ (e.g. Piran et al. 1993). Noticing $e \propto T'^4$ and the dynamical evolution eq.(13), one

can derive the comoving temperature at the photosphere radius r_{ph} as

$$T'_{\text{ph}} = \begin{cases} T_0 \left(\frac{r_{\text{ph}}}{r_0} \right)^{-1}, & r_0 < r_{\text{ph}} < r_{\text{ra}}; \\ T_0 \left(\frac{r_{\text{ra}}}{r_0} \right)^{-1} \left(\frac{r_{\text{ph}}}{r_{\text{ra}}} \right)^{-(2+\delta)/3}, & r_{\text{ra}} < r_{\text{ph}} < r_c; \\ T_0 \left(\frac{r_{\text{ra}}}{r_0} \right)^{-1} \left(\frac{r_c}{r_{\text{ra}}} \right)^{-(2+\delta)/3} \left(\frac{r_{\text{ph}}}{r_c} \right)^{-2/3}, & r_{\text{ph}} > r_c. \end{cases} \quad (22)$$

Here

$$T_0 \simeq \left(\frac{L_w}{4\pi r_0^2 a c (1 + \sigma_0)} \right)^{1/4} \quad (23)$$

is the temperature at r_0 , $a = 7.56 \times 10^{-15} \text{ erg cm}^{-3} \text{ K}^{-4}$ is radiation density constant. Given the central engine parameters L_w , r_0 , η and σ_0 , we can derive all the relevant photosphere properties with equations from (13) to (22), as long as the slow magnetic acceleration index δ is determined. The largest δ is $1/3$, which is achievable for an impulsive, non-dissipative magnetic shell (Granot et al. 2011). The general expressions for an arbitrary δ are presented in the Appendix. In the following, we present the results for $\delta = 1/3$. The implications of an arbitrary δ values are discussed in detail in Section 6. Also in the following analytical formulae, we have adopted $\Theta_{\text{ra}} = \Theta_c = 1$ (cold flow) and $\sigma_c = 0$ as a reasonable approximation.

For different central engine parameters, Γ_{ra} can have two possible values: η or $[\eta(1 + \sigma_0)]^{1/3}$. For each case, the photosphere radius r_{ph} can be in three different regimes separated by r_{ra} and r_c . So altogether we can define six different regimes: (I) $\eta > (1 + \sigma_0)^{1/2}$ and $r_{\text{ph}} < r_{\text{ra}}$; (II) $\eta > (1 + \sigma_0)^{1/2}$ and $r_{\text{ra}} < r_{\text{ph}} < r_c$; (III) $\eta > (1 + \sigma_0)^{1/2}$ and $r_{\text{ph}} > r_c$; (IV) $\eta < (1 + \sigma_0)^{1/2}$ and $r_{\text{ph}} < r_{\text{ra}}$; (V) $\eta < (1 + \sigma_0)^{1/2}$ and $r_{\text{ra}} < r_{\text{ph}} < r_c$; (VI) $\eta < (1 + \sigma_0)^{1/2}$ and $r_{\text{ph}} > r_c$. The six regimes also apply for the case with significant magnetic dissipation below the photosphere (see below). In Table 1, we list the criteria of all 12 regimes (for the cases of both without and with magnetic dissipations) based on the central engine properties. In the following, we derive relevant parameters in each regime, including r_{ra} and r_c (which are useful to write down the Γ evolution of the system), along with the photosphere properties, i.e. r_{ph} , Γ_{ph} , $(1 + \sigma_{\text{ph}})$, kT_{ob} , and F_{BB} :

Regime I:

$$\begin{aligned} r_{\text{ra}} &= 1.0 \times 10^{11} \text{ cm } r_{0,9} \eta_2, \\ r_c &= 1.0 \times 10^{17} \text{ cm } r_{0,9} \eta_2 (1 + \sigma_0)_2^3, \\ r_{\text{ph}} &= 8.34 \times 10^{10} \text{ cm } L_{w,52}^{1/3} r_{0,9}^{2/3} \eta_2^{-1/3} (1 + \sigma_0)_2^{-1/3}, \\ \Gamma_{\text{ph}} &= 83.4 L_{w,52}^{1/3} r_{0,9}^{-1/3} \eta_2^{-1/3} (1 + \sigma_0)_2^{-1/3}, \end{aligned}$$

$$\begin{aligned}
1 + \sigma_{\text{ph}} &= 100(1 + \sigma_0)_2, \\
kT_{\text{ob}} &= 56.1 \text{ keV } (1 + z)^{-1} L_{w,52}^{1/4} r_{0,9}^{-1/2} (1 + \sigma_0)_2^{-1/4}, \\
F_{\text{BB}} &= 1.07 \times 10^{-7} \text{ erg s}^{-1} \text{cm}^{-2} L_{w,52} (1 + \sigma_0)_2^{-1} d_{L,28}^{-2}.
\end{aligned} \tag{24}$$

Regime II:

$$\begin{aligned}
r_{\text{ra}} &= 1.0 \times 10^{11} \text{ cm } r_{0,9} \eta_2, \\
r_{\text{c}} &= 1.0 \times 10^{17} \text{ cm } r_{0,9} \eta_2 (1 + \sigma_0)_2^3, \\
r_{\text{ph}} &= 7.22 \times 10^{10} \text{ cm } L_{w,52}^{3/5} r_{0,9}^{2/5} \eta_2^{-7/5} (1 + \sigma_0)_2^{-3/5}, \\
\Gamma_{\text{ph}} &= 89.7 L_{w,52}^{1/5} r_{0,9}^{-1/5} \eta_2^{1/5} (1 + \sigma_0)_2^{-1/5}, \\
1 + \sigma_{\text{ph}} &= 17.7 L_{w,52}^{-1/5} r_{0,9}^{1/5} \eta_2^{4/5} (1 + \sigma_0)_2^{6/5}, \\
kT_{\text{ob}} &= 64.8 \text{ keV } (1 + z)^{-1} L_{w,52}^{-1/60} r_{0,9}^{-7/30} \eta_2^{16/15} (1 + \sigma_0)_2^{1/60}, \\
F_{\text{BB}} &= 1.24 \times 10^{-7} \text{ erg s}^{-1} \text{cm}^{-2} L_{w,52}^{11/15} r_{0,9}^{4/15} \eta_2^{16/15} (1 + \sigma_0)_2^{-11/15} d_{L,28}^{-2}.
\end{aligned} \tag{25}$$

Regime III:

$$\begin{aligned}
r_{\text{ra}} &= 1.0 \times 10^{11} \text{ cm } r_{0,9} \eta_2, \\
r_{\text{c}} &= 1.0 \times 10^{17} \text{ cm } r_{0,9} \eta_2 (1 + \sigma_0)_2^3, \\
r_{\text{ph}} &= 5.81 \times 10^{12} \text{ cm } L_{w,52} \eta_1^{-3} (1 + \sigma_0)_1^{-3}, \\
\Gamma_{\text{ph}} &= 100 \eta_1 (1 + \sigma_0)_1, \\
1 + \sigma_{\text{ph}} &\simeq 1, \\
kT_{\text{ob}} &= 6.65 \text{ keV } (1 + z)^{-1} L_{w,52}^{-5/12} r_{0,9}^{1/6} \eta_1^{8/3} (1 + \sigma_0)_1^{29/12}, \\
F_{\text{BB}} &= 7.15 \times 10^{-8} \text{ erg s}^{-1} \text{cm}^{-2} L_{w,52}^{1/3} r_{0,9}^{2/3} \eta_1^{8/3} (1 + \sigma_0)_1^{5/3} d_{L,28}^{-2}.
\end{aligned} \tag{26}$$

Regime IV:

$$\tag{27}$$

$$\begin{aligned}
r_{\text{ra}} &= 2.15 \times 10^{10} \text{ cm } r_{0,9} \eta_2^{1/3} (1 + \sigma_0)_2^{1/3}, \\
r_{\text{c}} &= 2.15 \times 10^{18} \text{ cm } r_{0,9} \eta_2^{7/3} (1 + \sigma_0)_2^{7/3}, \\
r_{\text{ph}} &= 8.34 \times 10^{10} \text{ cm } L_{w,52}^{1/3} r_{0,9}^{2/3} \eta_2^{-1/3} (1 + \sigma_0)_2^{-1/3}, \\
\Gamma_{\text{ph}} &= 83.4 L_{w,52}^{1/3} r_{0,9}^{-1/3} \eta_2^{-1/3} (1 + \sigma_0)_2^{-1/3}, \\
1 + \sigma_{\text{ph}} &= 5.56 L_{w,52}^{-1/3} r_{0,9}^{1/3} \eta_2^{4/3} (1 + \sigma_0)_2^{4/3}, \\
kT_{\text{ob}} &= 56.1 \text{ keV } (1 + z)^{-1} L_{w,52}^{1/4} r_{0,9}^{-1/2} (1 + \sigma_0)_2^{-1/4}, \\
F_{\text{BB}} &= 1.07 \times 10^{-7} \text{ erg s}^{-1} \text{ cm}^{-2} L_{w,52} (1 + \sigma_0)_2^{-1} d_{L,28}^{-2}.
\end{aligned} \tag{28}$$

Regime V:

$$\begin{aligned}
r_{\text{ra}} &= 2.15 \times 10^{10} \text{ cm } r_{0,9} \eta_2^{1/3} (1 + \sigma_0)_2^{1/3}, \\
r_{\text{c}} &= 2.15 \times 10^{18} \text{ cm } r_{0,9} \eta_2^{7/3} (1 + \sigma_0)_2^{7/3}, \\
r_{\text{ph}} &= 2.46 \times 10^{11} \text{ cm } L_{w,52}^{3/5} r_{0,9}^{2/5} \eta_2^{-13/15} (1 + \sigma_0)_2^{-13/15}, \\
\Gamma_{\text{ph}} &= 48.5 L_{w,52}^{1/5} r_{0,9}^{-1/5} \eta_2^{-1/15} (1 + \sigma_0)_2^{-1/15}, \\
1 + \sigma_{\text{ph}} &= 17.7 L_{w,52}^{-1/5} r_{0,9}^{1/5} \eta_2^{16/15} (1 + \sigma_0)_2^{16/15}, \\
kT_{\text{ob}} &= 19.0 \text{ keV } (1 + z)^{-1} L_{w,52}^{-1/60} r_{0,9}^{-7/30} \eta_2^{8/15} (1 + \sigma_0)_2^{17/60}, \\
F_{\text{BB}} &= 3.63 \times 10^{-8} \text{ erg s}^{-1} \text{ cm}^{-2} L_{w,52}^{11/15} r_{0,9}^{4/15} \eta_2^{8/15} (1 + \sigma_0)_2^{-7/15} d_{L,28}^{-2}.
\end{aligned} \tag{29}$$

Regime VI:

$$\begin{aligned}
r_{\text{ra}} &= 2.15 \times 10^{10} \text{ cm } r_{0,9} \eta_2^{1/3} (1 + \sigma_0)_2^{1/3}, \\
r_{\text{c}} &= 2.15 \times 10^{18} \text{ cm } r_{0,9} \eta_2^{7/3} (1 + \sigma_0)_2^{7/3}, \\
r_{\text{ph}} &= 5.81 \times 10^{12} \text{ cm } L_{w,52} \eta_1^{-3} (1 + \sigma_0)_1^{-3}, \\
\Gamma_{\text{ph}} &= 100 \eta_1 (1 + \sigma_0)_1, \\
1 + \sigma_{\text{ph}} &\simeq 1, \\
kT_{\text{ob}} &= 6.65 \text{ keV } (1 + z)^{-1} L_{w,52}^{-5/12} r_{0,9}^{1/6} \eta_1^{8/3} (1 + \sigma_0)_1^{29/12}, \\
F_{\text{BB}} &= 7.15 \times 10^{-8} \text{ erg s}^{-1} \text{ cm}^{-2} L_{w,52}^{1/3} r_{0,9}^{2/3} \eta_1^{8/3} (1 + \sigma_0)_1^{5/3} d_{L,28}^{-2}.
\end{aligned} \tag{30}$$

To better present our results, we show the contour plots of kT_{ob} and F_{BB} in the $(\eta, 1+\sigma_0)$ plane in Figure 2.

3.2. The case of magnetic dissipation

It has been speculated that significant magnetic dissipation may occur during the propagation of the jet below the photosphere. Such a magnetically dissipative photosphere (e.g. Thompson 1994; Rees & Mészáros 2005; Giannios 2008; Mészáros & Rees 2011; Veres & Mészáros 2012) would lead to enhancement of photosphere emission. On the other hand, the photosphere emission behavior is determined by the physical conditions far below the photosphere radius, where complete thermalization is not necessarily achieved without efficient creation of additional photons (Pe’er et al. 2006; Giannios 2006; Beloborodov 2010, 2013; Levinson 2012; Vurm et al. 2013; Bégué & Pe’er 2014). Specifically, for a dissipative photosphere due to magnetic dissipation, recent studies show that the photosphere emission could have a non-thermal appearance with a spectral peak (E_p) varying from 1 MeV up to a maximum value of about 20 MeV, depending on magnetization fraction σ_0 (Beloborodov 2013; Bégué & Pe’er 2014). Nonetheless, an *effective* temperature can be derived, which would be the temperature if the emission is fully thermalized (e.g. Eichler & Levinson 2000; Thompson et al. 2007). Practically, it would serve as an estimate of the *lower limit* of E_p of a magnetically dissipative photosphere emission. In this section, we quantify the photosphere emission properties under the assumption of significant magnetic dissipation.

With magnetic dissipation, the adiabatic relation no longer applies. One needs to introduce another conservation relation. One natural assumption is that the magnetic energy is converted into both thermal energy and kinetic energy of the bulk motion with fixed proportions (e.g. 1 : 1, but the exact proportions do not matter to define the temperature evolution of the system). With this assumption, in the lab frame and after the initial thermal acceleration phase, the internal energy should be proportional to Γ , so that in the comoving frame energy per baryon, $\Theta(r)$, should remain constant. This is translated to $r^2 e \Gamma = \text{const}$ (noticing that the co-moving size increases with Γ). In this case, the evolution of comoving temperature should be revised as

$$T'_{\text{ph}} = \begin{cases} T_0 \left(\frac{r_{\text{ph}}}{r_0} \right)^{-1}, & r_0 < r_{\text{ph}} < r_{\text{ra}}; \\ T_0 \left(\frac{r_{\text{ra}}}{r_0} \right)^{-1} \left(\frac{r_{\text{ph}}}{r_{\text{ra}}} \right)^{-(2+\delta)/4}, & r_{\text{ra}} < r_{\text{ph}} < r_{\text{c}}; \\ T_0 \left(\frac{r_{\text{ra}}}{r_0} \right)^{-1} \left(\frac{r_{\text{c}}}{r_{\text{ra}}} \right)^{-(2+\delta)/4} \left(\frac{r_{\text{ph}}}{r_{\text{c}}} \right)^{-2/3}, & r_{\text{ph}} > r_{\text{c}}. \end{cases} \quad (31)$$

Two remarks need to be made here. First, at $r_{\text{ph}} < r_{\text{ra}}$ (the first segment), there should be

a segment in which $T' \propto r^{-3/4}$ is satisfied. This is relevant for $\eta < (1 + \sigma_0)^{1/2}$ but at $r > r_0\eta$ (i.e. thermal acceleration is over and the flow is under rapid magnetic acceleration). The deviation from the approximate $T' \propto r^{-1}$ would be significant if $\eta \ll (1 + \sigma)^{1/2}$. However, in reality, a central engine always has a reasonably “hot” component so that $\eta \gg 1$. Also the introduction of this additional regime would not change the results substantially. We therefore do not get into the complications of introducing these trivial regimes. Second, at $r > r_c$, one has $\sigma < 1$. Heating due to magnetic dissipation becomes insignificant. One goes back to the scaling for an adiabatic outflow.

Using Eq.(31), we can similarly derive the relevant parameters for the six regimes in the magnetic dissipation case. Here $T_{\text{BB}}^{\text{eff}}$ is the effective temperature of the photosphere emission, so that $kT_{\text{BB}}^{\text{eff}}$ represents the lower limit of E_p of the dissipative photosphere emission. The corresponding effective blackbody flux is denoted as F_{ph} , which represents the νF_ν flux level for the photosphere emission. This flux level does not depend on the unknown E_p of the dissipative photosphere emission.

Regime I:

$$\begin{aligned}
 r_{\text{ra}} &= 1.0 \times 10^{11} \text{ cm } r_{0,9} \eta_2, \\
 r_c &= 1.0 \times 10^{17} \text{ cm } r_{0,9} \eta_2 (1 + \sigma_0)_2^3, \\
 r_{\text{ph}} &= 8.34 \times 10^{10} \text{ cm } L_{w,52}^{1/3} r_{0,9}^{2/3} \eta_2^{-1/3} (1 + \sigma_0)_2^{-1/3}, \\
 \Gamma_{\text{ph}} &= 83.4 L_{w,52}^{1/3} r_{0,9}^{-1/3} \eta_2^{-1/3} (1 + \sigma_0)_2^{-1/3}, \\
 1 + \sigma_{\text{ph}} &= 100(1 + \sigma_0)_2, \\
 kT_{\text{BB}}^{\text{eff}} &= 56.1 \text{ keV } (1 + z)^{-1} L_{w,52}^{1/4} r_{0,9}^{-1/2} (1 + \sigma_0)_2^{-1/4}, \\
 F_{\text{ph}} &= 1.07 \times 10^{-7} \text{ erg s}^{-1} \text{cm}^{-2} L_{w,52} (1 + \sigma_0)_2^{-1} d_{L,28}^{-2}.
 \end{aligned} \tag{32}$$

Regime II:

$$\begin{aligned}
 r_{\text{ra}} &= 1.0 \times 10^{11} \text{ cm } r_{0,9} \eta_2, \\
 r_c &= 1.0 \times 10^{17} \text{ cm } r_{0,9} \eta_2 (1 + \sigma_0)_2^3, \\
 r_{\text{ph}} &= 7.22 \times 10^{10} \text{ cm } L_{w,52}^{3/5} r_{0,9}^{2/5} \eta_2^{-7/5} (1 + \sigma_0)_2^{-3/5}, \\
 \Gamma_{\text{ph}} &= 89.7 L_{w,52}^{1/5} r_{0,9}^{-1/5} \eta_2^{1/5} (1 + \sigma_0)_2^{-1/5}, \\
 1 + \sigma_{\text{ph}} &= 17.7 L_{w,52}^{-1/5} r_{0,9}^{1/5} \eta_2^{4/5} (1 + \sigma_0)_2^{6/5},
 \end{aligned}$$

$$\begin{aligned}
kT_{\text{BB}}^{\text{eff}} &= 60.8 \text{ keV } (1+z)^{-1} L_{w,52}^{1/10} r_{0,9}^{-7/20} \eta_2^{3/5} (1+\sigma_0)_2^{-1/10}, \\
F_{\text{ph}} &= 9.62 \times 10^{-8} \text{ erg s}^{-1} \text{cm}^{-2} L_{w,52}^{6/5} r_{0,9}^{-1/5} \eta_2^{-4/5} (1+\sigma_0)_2^{-6/5} d_{L,28}^{-2}.
\end{aligned} \tag{33}$$

Regime III:

$$\begin{aligned}
r_{\text{ra}} &= 1.0 \times 10^{11} \text{ cm } r_{0,9} \eta_2, \\
r_{\text{c}} &= 1.0 \times 10^{17} \text{ cm } r_{0,9} \eta_2 (1+\sigma_0)_2^3, \\
r_{\text{ph}} &= 5.81 \times 10^{12} \text{ cm } L_{w,52} \eta_1^{-3} (1+\sigma_0)_1^{-3}, \\
\Gamma_{\text{ph}} &= 100 \eta_1 (1+\sigma_0)_1, \\
1 + \sigma_{\text{ph}} &\simeq 1, \\
kT_{\text{BB}}^{\text{eff}} &= 25.5 \text{ keV } (1+z)^{-1} L_{w,52}^{-5/12} r_{0,9}^{1/6} \eta_1^{8/3} (1+\sigma_0)_1^3, \\
F_{\text{ph}} &= 1.54 \times 10^{-5} \text{ erg s}^{-1} \text{cm}^{-2} L_{w,52}^{1/3} r_{0,9}^{2/3} \eta_1^{8/3} (1+\sigma_0)_1^4 d_{L,28}^{-2}.
\end{aligned} \tag{34}$$

Regime IV:

$$\begin{aligned}
r_{\text{ra}} &= 2.15 \times 10^{10} \text{ cm } r_{0,9} \eta_2^{1/3} (1+\sigma_0)_2^{1/3}, \\
r_{\text{c}} &= 2.15 \times 10^{18} \text{ cm } r_{0,9} \eta_2^{7/3} (1+\sigma_0)_2^{7/3}, \\
r_{\text{ph}} &= 8.34 \times 10^{10} \text{ cm } L_{w,52}^{1/3} r_{0,9}^{2/3} \eta_2^{-1/3} (1+\sigma_0)_2^{-1/3}, \\
\Gamma_{\text{ph}} &= 83.4 L_{w,52}^{1/3} r_{0,9}^{-1/3} \eta_2^{-1/3} (1+\sigma_0)_2^{-1/3}, \\
1 + \sigma_{\text{ph}} &= 5.56 L_{w,52}^{-1/3} r_{0,9}^{1/3} \eta_2^{4/3} (1+\sigma_0)_2^{4/3}, \\
kT_{\text{BB}}^{\text{eff}} &= 56.1 \text{ keV } (1+z)^{-1} L_{w,52}^{1/4} r_{0,9}^{-1/2} (1+\sigma_0)_2^{-1/4}, \\
F_{\text{ph}} &= 1.07 \times 10^{-7} \text{ erg s}^{-1} \text{cm}^{-2} L_{w,52} (1+\sigma_0)_2^{-1} d_{L,28}^{-2}.
\end{aligned} \tag{35}$$

Regime V:

$$\begin{aligned}
r_{\text{ra}} &= 2.15 \times 10^{10} \text{ cm } r_{0,9} \eta_2^{1/3} (1+\sigma_0)_2^{1/3}, \\
r_{\text{c}} &= 2.15 \times 10^{18} \text{ cm } r_{0,9} \eta_2^{7/3} (1+\sigma_0)_2^{7/3},
\end{aligned}$$

$$\begin{aligned}
r_{\text{ph}} &= 2.46 \times 10^{11} \text{ cm } L_{w,52}^{3/5} r_{0,9}^{2/5} \eta_2^{-13/15} (1 + \sigma_0)_2^{-13/15}, \\
\Gamma_{\text{ph}} &= 48.5 L_{w,52}^{1/5} r_{0,9}^{-1/5} \eta_2^{-1/15} (1 + \sigma_0)_2^{-1/15}, \\
1 + \sigma_{\text{ph}} &= 17.7 L_{w,52}^{-1/5} r_{0,9}^{1/5} \eta_2^{16/15} (1 + \sigma_0)_2^{16/15}, \\
kT_{\text{BB}}^{\text{eff}} &= 30.5 \text{ keV } (1 + z)^{-1} L_{w,52}^{1/10} r_{0,9}^{-7/20} \eta_2^{3/10} (1 + \sigma_0)_2^{1/20}, \\
F_{\text{ph}} &= 2.42 \times 10^{-7} \text{ erg s}^{-1} \text{ cm}^{-2} L_{w,52}^{6/5} r_{0,9}^{-1/5} \eta_2^{-2/5} (1 + \sigma_0)_2^{-7/5} d_{L,28}^{-2}.
\end{aligned} \tag{36}$$

Regime VI:

$$\begin{aligned}
r_{\text{ra}} &= 2.15 \times 10^{10} \text{ cm } r_{0,9} \eta_2^{1/3} (1 + \sigma_0)_2^{1/3}, \\
r_{\text{c}} &= 2.15 \times 10^{18} \text{ cm } r_{0,9} \eta_2^{7/3} (1 + \sigma_0)_2^{7/3}, \\
r_{\text{ph}} &= 5.81 \times 10^{12} \text{ cm } L_{w,52} \eta_1^{-3} (1 + \sigma_0)_1^{-3}, \\
1 + \Gamma_{\text{ph}} &= 100 \eta_1 (1 + \sigma_0)_1, \\
1 + \sigma_{\text{ph}} &\simeq 1, \\
kT_{\text{BB}}^{\text{eff}} &= 39.8 \text{ keV } (1 + z)^{-1} L_{w,52}^{-5/12} r_{0,9}^{1/6} \eta_1^{55/18} (1 + \sigma_0)_1^{101/36}, \\
F_{\text{ph}} &= 9.24 \times 10^{-5} \text{ erg s}^{-1} \text{ cm}^{-2} L_{w,52}^{1/3} r_{0,9}^{2/3} \eta_1^{38/9} (1 + \sigma_0)_1^{29/9} d_{L,28}^{-2}.
\end{aligned} \tag{37}$$

The criteria for different regimes are also presented in Table 1.

3.3. Example spectra

With the preparation above, one can simulate some example spectra of GRB prompt emission with the superposition of a photosphere emission component (which is thermal for a non-dissipative photosphere but could significantly deviate from the thermal form for a dissipative photosphere) and a non-thermal emission component from an optically thin region. Given a set of central engine parameters $(L_w, r_0, \eta, \sigma_0)$, the photosphere component can be quantified. A detailed simulation of the non-thermal component requires the assumptions of the explicit energy dissipation mechanism and radiation mechanism. For the purpose of this paper (which focuses on photosphere emission), we introduce the non-thermal component empirically. We take the non-thermal component as a Band function with typical observed parameters (Preece et al. 2000; Zhang et al. 2011; Nava et al. 2011): $E_{\text{peak}} = 1000 \text{ keV}$, $\alpha = -1$, and $\beta = -2.2$. The normalization of the spectrum is determined by assuming

that 50% of the remaining wind luminosity is converted to non-thermal emission. Such an efficiency may be relatively too high for IS model (e.g. Kumar 1999; Panaitescu et al. 1999), but would be reasonable for ICMART events (Zhang & Yan 2011). For a large parameter space, we find $\sigma > 1$ at 10^{15} cm, so that ICMART would be a more relevant energy dissipation mechanism for non-thermal emission (e.g. Fig.1). Even though no radiation mechanism is specified, we note that fast cooling synchrotron radiation at a relatively large emission radius is able to reproduce typical Band function spectra as observed (Uhm & Zhang 2014).

Some example spectra are presented in Figure 3 for different (η, σ_0) pairs as input parameters. For non-dissipative photosphere emission, we have assumed a blackbody spectrum. For dissipative photosphere emission, on the other hand, we only plot its flux level and the range of E_p defined by $kT_{\text{BB}}^{\text{eff}}$ and 20 MeV as suggested by Beloborodov (2013). One can see that a diversity of spectrum as observed by *Fermi* can be reproduced for the non-dissipative photosphere case, given that η and σ_0 are allowed to vary in a wide range. When $\sigma_0 \ll 1$ (panels (a-c), the fireball case), the photosphere emission is bright, and one would expect a bright thermal component sticking out from the Band component. This is consistent with the results of Zhang & Pe’er (2009) and Fan (2010). In particular, when η is large enough, the spectrum is completely dominated by the thermal component, similar to the case of GRB 090902B⁴. As η reduces or σ_0 increases (panels (d-i)), the photosphere component becomes sub-dominant (such as GRBs 100724B and 110721A), or even completely suppressed (such as GRB 080916C and many other bursts), as observed in many *Fermi* GRBs. For the cases with a large σ_0 , magnetic dissipation would enhance the photosphere emission as compared with the case without magnetic dissipation. However, if E_p of the dissipative photosphere emission is large, the predicted spectra are inconsistent with the Fermi data (Bégué & Pe’er 2014).

4. Inferring central engine parameters from the data: the top-down approach

In practice, a more interesting problem is to use the observed data to diagnose the properties at the central engine. Pe’er et al. (2007) worked out this problem for the pure fireball model. They pointed out that if $r_{\text{ph}} > r_c$, it is possible to derive η and r_0 based on the observed data. Due to a degeneracy, this is impossible if $r_{\text{ph}} \leq r_c$, which corresponds to a very large η value.

⁴The power law non-thermal emission as observed in GRB 090902B would require an additional spectral component, which may be related to inverse Compton scattering of some kind (Pe’er et al. 2012). This is not modeled in this paper.

In this section, we solve this problem for a more generalized hybrid outflow based on our results derived from the bottom-up approach. Since a blackbody component is predicted only in the non-dissipative photosphere model, our top-down approach only applies to the non-dissipative photosphere models. The magnetically dissipative photopshere models predict a much higher E_p , so they are disfavored by the data (Bégué & Pe’er 2014).

In general, one has three observed quantities: the observed blackbody temperature T_{ob} , the observed blackbody flux F_{BB} , and the observed total flux F_{ob} (both thermal and non-thermal included). In the pure fireball model, there are three unknowns: L_w , η , and r_0 . This is why Pe’er et al. (2007) can solve for η and r_0 from the data. In the hybrid problem, another parameter σ_0 is introduced, so that altogether there are four unknowns⁵. It is impossible to solve all four parameters from the data. On the other hand, applying the fireball method of Pe’er et al. (2007) to GRB 110721A led to curious, unreasonable parameters for η and r_0 as a function of t (Iyyani et al. 2013), suggesting that there are more parameters at play at the central engine. Physically, it is more reasonable to assume an essentially constant r_0 throughout a burst. Indeed, Ghirlanda et al. (2013) found that this is the case for some GRBs that are of a fireball origin. For hybrid systems, it is reasonable to assume a constant value for r_0 , and use the data to infer other three parameters. The results vary for different r_0 values.

In the following, we derive constraints on the central engine parameters η and σ_0 . We define $f_\gamma = L_\gamma/L_w$, which connects the total flux F_{ob} to the wind luminosity L_w . We also define $f_{\text{th}} = F_{\text{BB}}/F_{\text{ob}}$, which can be directly measured from the data. We then express η and σ_0 in terms of the measurables T_{ob} and f_{th} , along with f_γ and r_0 , both are taken as constants and can be estimated to a typical value (e.g. $f_\gamma = 0.5$, $r_0 = 10^8$ cm).

We also derive the radius of the photosphere r_{ph} , the Lorentz factor Γ_{ph} , and the magnetization parameter $(1 + \sigma_{\text{ph}})$ at the photosphere. In order to check whether IS or ICMART is responsible for the non-thermal emission, we also derive the magnetization parameter at $\sim 10^{15}$ cm, $(1 + \sigma_{15})$, based on a simple $\Gamma \propto r^{1/3}$ scaling law. If the derived $(1 + \sigma_{15})$ is smaller than 1, it means that 10^{15} cm is already in the coasting regime, and IS should be the main mechanism for non-thermal energy dissipation (e.g. Daigne et al. 2011). In this case, the real σ_{15} should be $\ll 1$, so that $(1 + \sigma_{15}) \simeq 1$. If the derived $(1 + \sigma_{15})$ is larger than 1, it suggests that significant non-thermal emission is generated through ICMART (Zhang & Yan 2011).

⁵In principle, the magnetic acceleration index δ might be another unknown parameter if it differs from $1/3$. In this work, we adopt $\delta = 1/3$ in the top-down approach and in the case study of GRB 110721A. The effect of a general δ value is discussed in detail at the end of Section 6.

We again consider the six regimes for the non-dissipative photosphere studied in section 3.1. Similar to Pe’er et al. (2007), Regimes I and IV ($r_{\text{ph}} < r_{\text{ra}}$) introduce an additional degeneracy, so that central engine parameters cannot be inferred. We therefore focus on the other four regimes. The criteria for the four regimes based on observations are summarized in Table 2.

For regime II, we have

$$\begin{aligned}
 1 + \sigma_0 &= 25.5(1+z)^{4/3} \left(\frac{kT_{\text{ob}}}{50 \text{ keV}} \right)^{4/3} \left(\frac{F_{\text{BB}}}{10^{-8} \text{ erg s}^{-1} \text{ cm}^{-2}} \right)^{-1/3} r_{0,9}^{2/3} f_{\text{th},-1}^{-1} f_{\gamma}^{-1} d_{L,28}^{-2/3}, \\
 \eta &= 74.8(1+z)^{11/12} \left(\frac{kT_{\text{ob}}}{50 \text{ keV}} \right)^{11/12} \left(\frac{F_{\text{BB}}}{10^{-8} \text{ erg s}^{-1} \text{ cm}^{-2}} \right)^{1/48} r_{0,9}^{5/24} d_{L,28}^{1/24}, \\
 r_{\text{ph}} &= 1.78 \times 10^{10} \text{ cm} (1+z)^{-25/12} \left(\frac{kT_{\text{ob}}}{50 \text{ keV}} \right)^{-25/12} \left(\frac{F_{\text{BB}}}{10^{-8} \text{ erg s}^{-1} \text{ cm}^{-2}} \right)^{37/48} r_{0,9}^{-7/24} d_{L,28}^{37/24}, \\
 \Gamma_{\text{ph}} &= 46.4(1+z)^{-1/12} \left(\frac{kT_{\text{ob}}}{50 \text{ keV}} \right)^{-1/12} \left(\frac{F_{\text{BB}}}{10^{-8} \text{ erg s}^{-1} \text{ cm}^{-2}} \right)^{13/48} r_{0,9}^{-7/24} d_{L,28}^{13/24}, \\
 1 + \sigma_{\text{ph}} &= 41.2(1+z)^{7/3} \left(\frac{kT_{\text{ob}}}{50 \text{ keV}} \right)^{7/3} \left(\frac{F_{\text{BB}}}{10^{-8} \text{ erg s}^{-1} \text{ cm}^{-2}} \right)^{-7/12} r_{0,9}^{7/6} f_{\text{th},-1}^{-1} f_{\gamma}^{-1} d_{L,28}^{-7/6}, \\
 1 + \sigma_{r_{15}} &= 1.08(1+z)^{59/36} \left(\frac{kT_{\text{ob}}}{50 \text{ keV}} \right)^{59/36} \left(\frac{F_{\text{BB}}}{10^{-8} \text{ erg s}^{-1} \text{ cm}^{-2}} \right)^{-47/144} r_{0,9}^{77/72} f_{\text{th},-1}^{-1} f_{\gamma}^{-1} d_{L,28}^{-47/72}.
 \end{aligned} \tag{38}$$

For regime III and VI, we have

$$\begin{aligned}
 1 + \sigma_0 &= 5.99(1+z)^{4/3} \left(\frac{kT_{\text{ob}}}{30 \text{ keV}} \right)^{4/3} \left(\frac{F_{\text{BB}}}{10^{-7} \text{ erg s}^{-1} \text{ cm}^{-2}} \right)^{-1/3} r_{0,9}^{2/3} f_{\text{th},-1}^{-1} f_{\gamma}^{-1} d_{L,28}^{-2/3}, \\
 \eta &= 20.3(1+z)^{-5/6} \left(\frac{kT_{\text{ob}}}{30 \text{ keV}} \right)^{-5/6} \left(\frac{F_{\text{BB}}}{10^{-7} \text{ erg s}^{-1} \text{ cm}^{-2}} \right)^{11/24} r_{0,9}^{-2/3} f_{\text{th},-1}^{3/4} f_{\gamma}^{3/4} d_{L,28}^{11/12}, \\
 r_{\text{ph}} &= 4.09 \times 10^{11} \text{ cm} (1+z)^{-3/2} \left(\frac{kT_{\text{ob}}}{30 \text{ keV}} \right)^{-3/2} \left(\frac{F_{\text{BB}}}{10^{-7} \text{ erg s}^{-1} \text{ cm}^{-2}} \right)^{5/8} f_{\text{th},-1}^{-1/4} f_{\gamma}^{-1/4} d_{L,28}^{5/4}, \\
 \Gamma_{\text{ph}} &= 121.3(1+z)^{1/2} \left(\frac{kT_{\text{ob}}}{30 \text{ keV}} \right)^{1/2} \left(\frac{F_{\text{BB}}}{10^{-7} \text{ erg s}^{-1} \text{ cm}^{-2}} \right)^{1/8} f_{\text{th},-1}^{-1/4} f_{\gamma}^{-1/4} d_{L,28}^{1/4}.
 \end{aligned} \tag{39}$$

For regime V, we have

$$\begin{aligned}
1 + \sigma_0 &= 6.43(1+z)^{4/3} \left(\frac{kT_{\text{ob}}}{10 \text{ keV}} \right)^{4/3} \left(\frac{F_{\text{BB}}}{10^{-9} \text{ erg s}^{-1} \text{ cm}^{-2}} \right)^{-1/3} r_{0,9}^{2/3} f_{\text{th},-1}^{-1} f_{\gamma}^{-1} d_{L,28}^{-2/3}, \\
\eta &= 105.0(1+z)^{7/6} \left(\frac{kT_{\text{ob}}}{10 \text{ keV}} \right)^{7/6} \left(\frac{F_{\text{BB}}}{10^{-9} \text{ erg s}^{-1} \text{ cm}^{-2}} \right)^{5/24} r_{0,9}^{1/12} f_{\text{th},-1}^{1/2} f_{\gamma}^{1/2} d_{L,28}^{5/12}, \\
r_{\text{ph}} &= 4.62 \times 10^{10} \text{ cm} (1+z)^{-13/6} \left(\frac{kT_{\text{ob}}}{10 \text{ keV}} \right)^{-13/6} \left(\frac{F_{\text{BB}}}{10^{-9} \text{ erg s}^{-1} \text{ cm}^{-2}} \right)^{17/24} r_{0,9}^{-1/4} f_{\text{th},-1}^{-1/6} f_{\gamma}^{-1/6} d_{L,28}^{17/12}, \\
\Gamma_{\text{ph}} &= 15.3(1+z)^{-1/6} \left(\frac{kT_{\text{ob}}}{10 \text{ keV}} \right)^{-1/6} \left(\frac{F_{\text{BB}}}{10^{-9} \text{ erg s}^{-1} \text{ cm}^{-2}} \right)^{5/24} r_{0,9}^{-1/4} f_{\text{th},-1}^{-1/6} f_{\gamma}^{-1/6} d_{L,28}^{5/12}, \\
1 + \sigma_{\text{ph}} &= 44.2(1+z)^{8/3} \left(\frac{kT_{\text{ob}}}{10 \text{ keV}} \right)^{8/3} \left(\frac{F_{\text{BB}}}{10^{-9} \text{ erg s}^{-1} \text{ cm}^{-2}} \right)^{-1/3} r_{0,9} f_{\text{th},-1}^{-1/3} f_{\gamma}^{-1/3} d_{L,28}^{-2/3}, \\
1 + \sigma_{r_{15}} &= 1.59(1+z)^{35/18} \left(\frac{kT_{\text{ob}}}{10 \text{ keV}} \right)^{35/18} \left(\frac{F_{\text{BB}}}{10^{-9} \text{ erg s}^{-1} \text{ cm}^{-2}} \right)^{-7/72} r_{0,9}^{11/12} f_{\text{th},-1}^{-7/18} f_{\gamma}^{-7/18} d_{L,28}^{-7/36}.
\end{aligned} \tag{40}$$

Notice that regime VI has the identical scalings as regime III.

5. Case study: GRB 110721A

GRB 110721A was jointly detected by the *Fermi* GBM and LAT. Axelsson et al. (2012) reported the time-dependent spectral evolution of GRB 110721A and suggested that the time-resolved emission spectra are best modeled with a combination of a Band function and a blackbody component. Based on a candidate optical counterpart (Greiner et al. 2011), Berger (2011) suggested two possible redshifts, $z = 0.382$ or $z = 3.512$, with the former preferred.

Iyyani et al. (2013) analyzed the time-resolved data of GRB 110721A and presented the time-dependent properties (including $f_{\text{th}} = F_{\text{BB}}/F_{\text{ob}}$, panel (a) of Fig.4; T_{ob} , and $(F_{\text{BB}}/\sigma T_{\text{ob}}^4)^{1/2}$, panel (b) of Fig.4). Based on the diagnostic method of Pe’er et al. (2007), they derived $\eta(t)$ and $r_0(t)$. Some uncomfortable conclusions were obtained: First, $\eta(t)$ decreases with time. This is at odds with the IS model, which demands a time-increasing $\eta(t)$ to make strong ISs and efficient non-thermal emission. Second, r_0 was found to increase by more than two orders of magnitude early on and later decrease by near one order of magnitude. It is hard to imagine any realistic central engine that may change its size with such a large amplitude in such a short period of time.

By applying our top-down diagnostic method, the data can be naturally explained

(Fig.4). We find that in all time bins, one has $(1 + \sigma_0) \gg 1$, so that the Pe’er et al. (2007) approach cannot be applied. The variation of the thermal emission properties in the time-resolved spectra is a result of varying (η, σ_0) pair as a function of time at the central engine. This is a more reasonable conclusion as compared with the varying r_0 result. The GRB central engine is highly erratic, so that it is possible that the dimensionless entropy and magnetization can vary noticeably with time. Our inferred parameters depend on the assumed constant r_0 . In Fig.4 (panels c,d), we present the results of $(1 + \sigma_0)$ and η as a function of time for three assumed r_0 : 10^8 (plus), 10^9 (square), and 10^{10} (cross) cm. We also plot the photosphere radius r_{ph} and photosphere Lorentz factor Γ_{ph} as a function of t for all the cases (panels (e,f) of Fig.4). It is interesting to see that the derived $(1 + \sigma_0)$ initially increases with time, which is consistent with the expectation of some central engine models (e.g. Metzger et al. 2011, W.-H. Lei et al. 2014, in preparation). It is also interesting to note that Γ_{ph} initially rises with time, in contrast to the case of the pure fireball model (Iyyani et al. 2013). This is a more natural picture for both IS and ICMART scenarios. For this case, $(1 + \sigma_{15})$ is found to be above unity for some time bins. This suggests that ICMART rather than IS is the mechanism to power the non-thermal emission for at least some, and probably all time bins (even if σ_{15} is smaller, but not much smaller than unity, IS is still inefficient, and ICMART can enhance energy dissipation). Based on the results in Section 4, we find that $(1 + \sigma_{15})$ tends to be larger for a larger r_0 . This is confirmed from the analysis of this burst.

6. Conclusions and Discussion

The central engine of GRB jets is most likely a hybrid system with both a hot fireball component and a cold Poynting flux component. In this work, we developed an analytical theory to quantify the properties of the photosphere emission of such a hybrid system. Based on an approximate dynamical evolution model of the hybrid system, we developed a “bottom-up” approach to predict the temperature and luminosity of the photosphere emission for arbitrary input parameters, especially η and σ_0 . We consider the cases of both with and without significant magnetic dissipation below the photosphere. We show that a variety of observed GRB prompt emission spectra by *Fermi* can be reproduced for the non-dissipative photosphere model, given that η and σ_0 are allowed to vary in a wide range (Fig.3). We also developed a “top-down” approach to diagnose η and σ_0 within the non-dissipative photosphere model using the observations that show a superposed blackbody component in the GRB spectra. We apply the method to GRB 110721A and draw the conclusion that the central engine of the source as well as its photosphere is highly magnetized, and that the non-thermal emission is likely produced via magnetic dissipation (ICMART)

rather than internal shocks. The rapid evolution of the photosphere emission properties is a result of rapid evolution of (η, σ_0) pairs rather than rapid evolution of r_0 (cf. Iyyani et al. 2013). We recommend to apply our method to diagnose a large sample of *Fermi* GRBs with the detected photosphere component, so as to carry out a statistical analysis of the central engine properties of a large sample of GRBs. This would have interesting implications in diagnosing the composition of GRB jets as well as inferring the mechanisms of GRB jet energy dissipation and radiation.

It is useful to comment on the relationship between our work and several previous papers. Pe’er et al. (2007) were the first to propose to diagnose central engine parameters using the observed photosphere emission properties. Their method is within the standard fireball framework. Our general diagnostic method is consistent with Pe’er et al. (2007) when $\sigma_0 \ll 1$ is assumed. Veres & Mészáros (2012) introduced the slow acceleration segment in a magnetically dominated flow to calculate the properties of the dissipative photosphere. Their photosphere radius is within the $\Gamma \propto R^{1/3}$ regime (i.e. our regimes II and V). However, they did not introduce the $(1 + \sigma_0)$ parameter to suppress the photosphere luminosity. This would over-estimate the photosphere brightness in more general cases. Hascoët et al. (2013) introduced a parameter to denote the fraction of thermal energy at the central engine, and calculated the brightness of the photosphere emission. However, they did not explicitly take into account the dynamical evolution of a high- σ outflow. As shown in this paper, in order to reproduce the photosphere properties of the data (or upper limits), σ_0 is such that the coasting radius is usually above the IS radius. This suggests that ISs cannot operate efficiently, and significant jet energy dissipation has to proceed through magnetic dissipation processes such as ICMART. Based on the theoretical framework of Hascoët et al. (2013), Guiriec et al. (2013) presented a method to infer r_0 , η and r_{ph} using observed quantities (their eqs.(3-5)). Their results agree with our regimes III and VI without magnetic dissipation (the coasting regime). They applied the method to the short GRB 120323A and obtained an anomalously low γ -ray efficiency. It is likely that the photosphere radius is in the slow magnetic acceleration regime, so that their diagnostic method should be replaced by ours in the regimes II and V. This would alleviate the low efficiency problem encountered by the burst. Finally, Peng et al. (2014) recently discovered a sub-dominant thermal component in the X-ray flares of some GRBs with a typical temperature of a few keV. According to Figures 2, a low temperature, low flux thermal component typically requires a large σ_0 . This is consistent with the theoretical argument that a magnetic mechanism has to play an important role to power an X-ray flare jet (Fan et al. 2005).

Finally, we’d like to point out several caveats of our approach. First, we have introduced a simple toy model to describe the dynamical evolution of a hybrid jet. We have assumed that the jet is accelerated initially thermally and later magnetically. Such a treatment was

adopted by Mészáros & Rees (1997), and was proven to be valid for a specific hybrid MHD jet model Vlahakis & Königl (2003). We assume a linear acceleration below a “rapid acceleration” radius r_{ra} defined by the maximum of thermal coasting radius and the magneto-sonic point. We argue that this approximation is good for a hybrid jet. However, in reality the acceleration of a hybrid system in the rapid acceleration phase should be more complicated, requiring to solve a set of MHD equations with the contribution of a radiation force (e.g. Russo & Thompson 2013). The solution may deviate from the simple linear acceleration assumption adopted here. If future detailed numerical simulations show deviation from this simple linear acceleration law below r_{ra} , both of our bottom-up and top-down approaches should be modified accordingly. Another complication is the possible additional acceleration due to collimation of a stellar envelope (Tchekhovskoy et al. 2009, 2010). We argue that after the jet breaks out from the star, the confinement profile adopted by Tchekhovskoy et al. (2010), which is valid during jet propagation inside the star (Zhang et al. 2003), would be modified, so that the additional acceleration effect may not be significant. Our treatment neglected this effect. If it turns out that this effect is significant, then our treatment should be improved to include this correction effect. In any case, since in most cases r_{ph} is above r_{ra} , the approaches derived here should give correct results to order of magnitude.

A final uncertainty of our approach is the acceleration index δ during the slow acceleration phase. For the bottom-up approach, we derived results for the arbitrary δ case (presented in the Appendix), but presented in the main text the $\delta = 1/3$ case. For the top-down approach, we only derived the formulae for the $\delta = 1/3$ case. For the non-dissipative photosphere model we focus in the paper, such an acceleration law may be achieved for an impulsive jet, as is the case for GRBs (Granot et al. 2011). Nonetheless, a shallower acceleration law with $\delta < 1/3$ may be possible, which would lead to corrections to the results from the $\delta = 1/3$ model. In Figure 5, we show how the photosphere properties vary with δ . It turns out that the ratio $T_{\text{ob}}(\delta)/T_{\text{ob}}(1/3)$ is the same as the ratio $F_{\text{BB}}(\delta)/F_{\text{BB}}(1/3)$, which varies by a factor of 50% as long as δ is not too small (say, above 0.2). In most cases that are relevant to GRBs (e.g. $100 < \eta(1 + \sigma_0) < 10000$), the temperature and flux derived with $\delta = 1/3$ set an upper limit for the more general δ models. In any case, with $\delta < 1/3$, magnetic acceleration is less efficient during the slow acceleration regime, so that it is even more difficult to reach the coasting phase before deceleration. The parameter space for internal shocks to operate is further reduced, and it is more likely that ICMART is the main mechanism to power bright non-thermal emission from GRBs.

We thank Peter Mészáros, Asaf Pe’er, Robert Mochkovitch, and Z. Lucas Uhm for helpful comments, and an anonymous referee for a constructive report. This work is partially supported by NASA through grant NNX14AF85G.

REFERENCES

- Abdo, A. A., Ackermann, M., Ajello, M., et al. 2009a, *ApJ*, 706, L138
- Abdo, A. A., Ackermann, M., Arimoto, M., et al. 2009b, *Science*, 323, 1688
- Atwood, W. B., Abdo, A. A., Ackermann, M., et al. 2009, *ApJ*, 697, 1071
- Axelsson, M., Baldini, L., Barbiellini, G., et al. 2012, *ApJ*, 757, L31
- Band, D., Matteson, J., Ford, L., et al. 1993, *ApJ*, 413, 281
- Bégué, D., & Pe’er, A. 2014, arXiv:1410.2730
- Beloborodov, A. M. 2010, *MNRAS*, 407, 1033
- Beloborodov, A. M. 2013, *ApJ*, 764, 157
- Berger, E. 2011, *GRB Coordinates Network*, 12193, 1
- Daigne, F., & Mochkovitch, R. 1998, *MNRAS*, 296, 275
- Daigne, F., & Mochkovitch, R. 2002, *MNRAS*, 336, 1271
- Daigne, F., Bošnjak, Ž., & Dubus, G. 2011, *A&A*, 526, A110
- Deng, W., & Zhang, B. 2014, *ApJ*, 785, 112
- Drenkhahn, G., & Spruit, H. C. 2002, *A&A*, 391, 1141
- Eichler, D., & Levinson, A. 2000, *ApJ*, 529, 146
- Fan, Y. Z., Zhang, B., & Proga, D. 2005, *ApJ*, 635, L129
- Fan, Y.-Z. 2010, *MNRAS*, 403, 483
- Ghirlanda, G., Celotti, A., & Ghisellini, G. 2002, *A&A*, 393, 409
- Ghirlanda, G., Celotti, A., & Ghisellini, G. 2003, *A&A*, 406, 879
- Ghirlanda, G., Pescalli, A., & Ghisellini, G. 2013, *MNRAS*, 432, 3237
- Giannios, D. 2006, *A&A*, 457, 763
- Giannios, D. 2008, *A&A*, 480, 305
- Giannios, D. 2012, *MNRAS*, 422, 3092

- Goodman, J. 1986, *ApJ*, 308, L47
- Granot, J., Komissarov, S. S., & Spitkovsky, A. 2011, *MNRAS*, 411, 1323
- Granot, J. 2012, *MNRAS*, 421, 2442
- Greiner, J., Utdike, A. C., Kruehler, T., & Sudilovsky, V. 2011, GRB Coordinates Network, 12192, 1
- Guiriec, S., Connaughton, V., Briggs, M. S., et al. 2011, *ApJ*, 727, L33
- Guiriec, S., Daigne, F., Hascoët, R., et al. 2013, *ApJ*, 770, 32
- Hascoët, R., Daigne, F., & Mochkovitch, R. 2013, *A&A*, 551, A124
- Ioka, K. 2010, *Progress of Theoretical Physics*, 124, 667
- Iyyani, S., Ryde, F., Axelsson, M., et al. 2013, *MNRAS*, 433, 2739
- Komissarov, S. S., Vlahakis, N., Königl, A., & Barkov, M. V. 2009, *MNRAS*, 394, 1182
- Kumar, P. 1999, *ApJ*, 523, L113
- Kumar, P., & Zhang, B. 2015, *Phys. Rep.*, in press (arXiv:1410.0679)
- Lazzati, D., & Begelman, M. C. 2010, *ApJ*, 725, 1137
- Lei, W.-H., Zhang, B., & Liang, E.-W. 2013, *ApJ*, 765, 125
- Levinson, A. 2012, *ApJ*, 756, 174
- Li, Z.-Y., Chiueh, T., & Begelman, M. C. 1992, *ApJ*, 394, 459
- Li, Z., & Waxman, E. 2008, *ApJ*, 674, L65
- Lloyd, N. M., & Petrosian, V. 2000, *ApJ*, 543, 722
- Lundman, C., Pe’er, A., & Ryde, F. 2013, *MNRAS*, 428, 2430
- Lyutikov, M., & Blandford, R. 2003, arXiv:astro-ph/0312347
- Mészáros, P., Laguna, P., & Rees, M. J. 1993, *ApJ*, 415, 181
- Mészáros, P., & Rees, M. J. 1993, *ApJ*, 405, 278
- Mészáros, P., Rees, M. J., & Papathanassiou, H. 1994, *ApJ*, 432, 181

- Mészáros, P., & Rees, M. J. 1997, *ApJ*, 482, L29
- Mészáros, P., & Rees, M. J. 2000, *ApJ*, 530, 292
- Mészáros, P., Ramirez-Ruiz, E., Rees, M. J., & Zhang, B. 2002, *ApJ*, 578, 812
- Mészáros, P., & Rees, M. J. 2011, *ApJ*, 733, L40
- Meegan, C., Lichti, G., Bhat, P. N., et al. 2009, *ApJ*, 702, 791
- Metzger, B. D., Giannios, D., Thompson, T. A., Bucciantini, N., & Quataert, E. 2011, *MNRAS*, 413, 2031
- Nava, L., Ghirlanda, G., Ghisellini, G., & Celotti, A. 2011, *A&A*, 530, A21
- Paczynski, B. 1986, *ApJ*, 308, L43
- Panaitescu, A., Spada, M., & Mészáros, P. 1999, *ApJ*, 522, L105
- Pe’er, A., Mészáros, P., & Rees, M. J. 2006, *ApJ*, 642, 995
- Pe’er, A., Ryde, F., Wijers, R. A. M. J., Mészáros, P., & Rees, M. J. 2007, *ApJ*, 664, L1
- Pe’er, A., & Ryde, F. 2011, *ApJ*, 732, 49
- Pe’Er, A., Zhang, B.-B., Ryde, F., et al. 2012, *MNRAS*, 420, 468
- Peng, F.-K., Liang, E.-W., Wang, X.-Y., et al. 2014, *ApJ* Submitted
- Piran, T., Shemi, A., & Narayan, R. 1993, *MNRAS*, 263, 861
- Preece, R. D., Briggs, M. S., Mallozzi, R. S., et al. 2000, *ApJS*, 126, 19
- Preece, R., Burgess, J. M., von Kienlin, A., et al. 2014, *Science*, 343, 51
- Rees, M. J., & Mészáros, P. 1992, *MNRAS*, 258, 41P
- Rees, M. J., & Mészáros, P. 1994, *ApJ*, 430, L93
- Rees, M. J., & Mészáros, P. 2005, *ApJ*, 628, 847
- Russo, M., & Thompson, C. 2013, *ApJ*, 773, 99
- Ryde, F. 2005, *ApJ*, 625, L95
- Ryde, F., & Pe’er, A. 2009, *ApJ*, 702, 1211

- Ryde, F., Axelsson, M., Zhang, B. B., et al. 2010, *ApJ*, 709, L172
- Shemi, A., & Piran, T. 1990, *ApJ*, 365, L55
- Spruit, H. C., Daigne, F., & Drenkhahn, G. 2001, *A&A*, 369, 694
- Tavani, M. 1996, *ApJ*, 466, 768
- Tchekhovskoy, A., McKinney, J. C., & Narayan, R. 2009, *ApJ*, 699, 1789
- Tchekhovskoy, A., Narayan, R., & McKinney, J. C. 2010, *New A*, 15, 749
- Thompson, C. 1994, *MNRAS*, 270, 480
- Thompson, C., Mészáros, P., & Rees, M. J. 2007, *ApJ*, 666, 1012
- Uhm, Z. L., & Zhang, B. 2014, *Nature Physics*, 10, 351
- Usov, V. V. 1994, *MNRAS*, 267, 1035
- Uzdensky, D. A., & MacFadyen, A. I. 2006, *ApJ*, 647, 1192
- Veres, P., & Mészáros, P. 2012, *ApJ*, 755, 12
- Veres, P., Zhang, B.-B., & Mészáros, P. 2012, *ApJ*, 761, L18
- Vlahakis, N., & Königl, A. 2003, *ApJ*, 596, 1104
- Vurm, I., Beloborodov, A. M., & Poutanen, J. 2011, *ApJ*, 738, 77
- Vurm, I., Lyubarsky, Y., & Piran, T. 2013, *ApJ*, 764, 143
- Yuan, F., & Zhang, B. 2012, *ApJ*, 757, 56
- Zhang, B., & Mészáros, P. 2002, *ApJ*, 581, 1236
- Zhang, B., & Pe’er, A. 2009, *ApJ*, 700, L65
- Zhang, B., & Yan, H. 2011, *ApJ*, 726, 90
- Zhang, B. 2011, *Comptes Rendus Physique*, 12, 206
- Zhang, B., Lu, R.-J., Liang, E.-W., & Wu, X.-F. 2012, *ApJ*, 758, L34
- Zhang, B. 2014, *International Journal of Modern Physics D*, 23, 30002
- Zhang, B., & Zhang, B. 2014, *ApJ*, 782, 92

Zhang, B.-B., Zhang, B., Liang, E.-W., et al. 2011, ApJ, 730, 141

Zhang, W., Woosley, S. E., MacFadyen, A. I. 2003, ApJ, 586, 356

Appendix

In this Appendix, we present the results for an arbitrary δ value. The corresponding expressions in regimes II and V in Section 3.1 read the following:

Regime II:

$$\begin{aligned}
 r_{\text{ra}} &= 1.0 \times 10^{11} \text{ cm } r_{0,9} \eta_2, \\
 r_{\text{c}} &= 1.0 \times 10^{\frac{11\delta+2}{\delta}} \text{ cm } r_{0,9} \eta_2 (1 + \sigma_0)_2^{\frac{1}{\delta}}, \\
 r_{\text{ph}} &= 5.8 \times 10^{\frac{22\delta+10}{2\delta+1}} \text{ cm } L_{w,52}^{\frac{1}{2\delta+1}} r_{0,9}^{\frac{2\delta}{2\delta+1}} \eta_2^{\frac{2\delta-3}{2\delta+1}} (1 + \sigma_0)_2^{-\frac{1}{2\delta+1}}, \\
 \Gamma_{\text{ph}} &= 5.8 \times 10^{\frac{3\delta+2}{2\delta+1}} L_{w,52}^{\frac{\delta}{2\delta+1}} r_{0,9}^{-\frac{\delta}{2\delta+1}} \eta_2^{\frac{1-2\delta}{2\delta+1}} (1 + \sigma_0)_2^{-\frac{\delta}{2\delta+1}}, \\
 1 + \sigma_{\text{ph}} &= 10^{\frac{19\delta+2}{2\delta+1}} e^{-\frac{43.2\delta}{2\delta+1}} L_{w,52}^{-\frac{\delta}{2\delta+1}} r_{0,9}^{\frac{\delta}{2\delta+1}} \eta_2^{\frac{4\delta}{2\delta+1}} (1 + \sigma_0)_2^{\frac{3\delta+1}{2\delta+1}}, \\
 kT_{\text{ob}} &= 1.2 \times 10^{\frac{43-28\delta}{6\delta+3}} e^{\frac{86.4\delta-86.4}{6\delta+3}} \text{ keV } (1+z)^{-1} L_{w,52}^{\frac{14\delta-5}{24\delta+12}} r_{0,9}^{\frac{1-10\delta}{12\delta+6}} \eta_2^{\frac{8-8\delta}{6\delta+3}} (1 + \sigma_0)_2^{\frac{5-14\delta}{24\delta+12}}, \\
 F_{\text{BB}} &= 2.3 \times 10^{\frac{16-82\delta}{6\delta+3}} e^{\frac{86.4\delta-86.4}{6\delta+3}} \text{ erg s}^{-1} \text{ cm}^{-2} L_{w,52}^{\frac{8\delta+1}{6\delta+3}} r_{0,9}^{\frac{2-2\delta}{6\delta+3}} \eta_2^{\frac{8-8\delta}{6\delta+3}} (1 + \sigma_0)_2^{-\frac{8\delta+1}{6\delta+3}} d_{L,28}^{-2}.
 \end{aligned} \tag{1}$$

Regime V:

$$\begin{aligned}
 r_{\text{ra}} &= 2.15 \times 10^{10} \text{ cm } r_{0,9} \eta_2^{1/3} (1 + \sigma_0)_2^{1/3}, \\
 r_{\text{c}} &= 2.15 \times 10^{\frac{31\delta+8}{3\delta}} \text{ cm } r_{0,9} \eta_2^{\frac{\delta+2}{3\delta}} (1 + \sigma_0)_2^{\frac{\delta+2}{3\delta}}, \\
 r_{\text{ph}} &= 5.8 \times 10^{\frac{62\delta+34}{6\delta+3}} \text{ cm } L_{w,52}^{\frac{1}{2\delta+1}} r_{0,9}^{\frac{2\delta}{2\delta+1}} \eta_2^{\frac{2\delta-5}{6\delta+3}} (1 + \sigma_0)_2^{\frac{2\delta-5}{6\delta+3}}, \\
 \Gamma_{\text{ph}} &= 5.8 \times 10^{\frac{11\delta+4}{6\delta+3}} L_{w,52}^{\frac{\delta}{2\delta+1}} r_{0,9}^{-\frac{\delta}{2\delta+1}} \eta_2^{\frac{1-4\delta}{6\delta+3}} (1 + \sigma_0)_2^{\frac{1-4\delta}{6\delta+3}}, \\
 1 + \sigma_{\text{ph}} &= 10^{\frac{19\delta+2}{2\delta+1}} e^{-\frac{43.2\delta}{2\delta+1}} L_{w,52}^{-\frac{\delta}{2\delta+1}} r_{0,9}^{\frac{\delta}{2\delta+1}} \eta_2^{\frac{10\delta+2}{6\delta+3}} (1 + \sigma_0)_2^{\frac{10\delta+2}{6\delta+3}}, \\
 kT_{\text{ob}} &= 4.3 \times 10^{\frac{112-82\delta}{18\delta+9}} e^{\frac{86.4\delta-86.4}{6\delta+3}} \text{ keV } (1+z)^{-1} L_{w,52}^{\frac{14\delta-5}{24\delta+12}} r_{0,9}^{\frac{1-10\delta}{12\delta+6}} \eta_2^{\frac{4-4\delta}{6\delta+3}} (1 + \sigma_0)_2^{\frac{13-22\delta}{24\delta+12}}, \\
 F_{\text{BB}} &= 0.83 \times 10^{\frac{40-226\delta}{18\delta+9}} e^{\frac{86.4\delta-86.4}{6\delta+3}} \text{ erg s}^{-1} \text{ cm}^{-2} L_{w,52}^{\frac{8\delta+1}{6\delta+3}} r_{0,9}^{\frac{2-2\delta}{6\delta+3}} \eta_2^{\frac{4-4\delta}{6\delta+3}} (1 + \sigma_0)_2^{\frac{1-10\delta}{6\delta+3}} d_{L,28}^{-2}.
 \end{aligned} \tag{2}$$

Similarly, the corresponding expressions for Regimes II, III, V, and VI in Section 3.2 read the following:

Regime II

$$r_{\text{ra}} = 1.0 \times 10^{11} \text{ cm } r_{0,9} \eta_2,$$

$$\begin{aligned}
r_c &= 1.0 \times 10^{\frac{11\delta+2}{\delta}} \text{ cm } r_{0,9} \eta_2 (1 + \sigma_0)_2^{\frac{1}{\delta}}, \\
r_{\text{ph}} &= 5.8 \times 10^{\frac{22\delta+10}{2\delta+1}} \text{ cm } L_{w,52}^{\frac{1}{2\delta+1}} r_{0,9}^{\frac{2\delta}{2\delta+1}} \eta_2^{\frac{2\delta-3}{2\delta+1}} (1 + \sigma_0)_2^{-\frac{1}{2\delta+1}}, \\
\Gamma_{\text{ph}} &= 5.8 \times 10^{\frac{3\delta+2}{2\delta+1}} L_{w,52}^{\frac{\delta}{2\delta+1}} r_{0,9}^{-\frac{\delta}{2\delta+1}} \eta_2^{\frac{1-2\delta}{2\delta+1}} (1 + \sigma_0)_2^{-\frac{\delta}{2\delta+1}}, \\
1 + \sigma_{\text{ph}} &= 10^{\frac{19\delta+2}{2\delta+1}} e^{-\frac{43.2\delta}{2\delta+1}} L_{w,52}^{-\frac{\delta}{2\delta+1}} r_{0,9}^{\frac{\delta}{2\delta+1}} \eta_2^{\frac{4\delta}{2\delta+1}} (1 + \sigma_0)_2^{\frac{3\delta+1}{2\delta+1}}, \\
kT_{\text{BB}}^{\text{eff}} &= 1.8 \times 10^{\frac{44-45\delta}{8\delta+4}} e^{\frac{129.6\delta-86.4}{8\delta+4}} \text{ keV } (1+z)^{-1} L_{w,52}^{\frac{5\delta-1}{8\delta+4}} r_{0,9}^{-\frac{7\delta}{8\delta+4}} \eta_2^{\frac{2-3\delta}{2\delta+1}} (1 + \sigma_0)_2^{\frac{1-5\delta}{8\delta+4}}, \\
F_{\text{ph}} &= 5.8 \times 10^{-\frac{15\delta+7}{2\delta+1}} \text{ erg s}^{-1} \text{ cm}^{-2} L_{w,52}^{\frac{3\delta+1}{2\delta+1}} r_{0,9}^{-\frac{\delta}{2\delta+1}} \eta_2^{-\frac{4\delta}{2\delta+1}} (1 + \sigma_0)_2^{-\frac{3\delta+1}{2\delta+1}} d_{L,28}^{-2}.
\end{aligned} \tag{3}$$

Regime III:

$$\begin{aligned}
r_{\text{ra}} &= 1.0 \times 10^{11} \text{ cm } r_{0,9} \eta_2, \\
r_c &= 1.0 \times 10^{\frac{11\delta+2}{\delta}} \text{ cm } r_{0,9} \eta_2 (1 + \sigma_0)_2^{\frac{1}{\delta}}, \\
r_{\text{ph}} &= 5.81 \times 10^{12} \text{ cm } L_{w,52} \eta_1^{-3} (1 + \sigma_0)_1^{-3}, \\
\Gamma_{\text{ph}} &= 100 \eta_1 (1 + \sigma_0)_1, \\
1 + \sigma_{\text{ph}} &\simeq 1, \\
kT_{\text{BB}}^{\text{eff}} &= 8.1 \times 10^{\frac{1}{6\delta}} \text{ keV } (1+z)^{-1} L_{w,52}^{-5/12} r_{0,9}^{1/6} \eta_1^{8/3} (1 + \sigma_0)_1^{\frac{15\delta+1}{6\delta}}, \\
F_{\text{ph}} &= 1.54 \times 10^{\frac{2-21\delta}{3\delta}} \text{ erg s}^{-1} \text{ cm}^{-2} L_{w,52}^{1/3} r_{0,9}^{2/3} \eta_1^{8/3} (1 + \sigma_0)_1^{\frac{6\delta+2}{3\delta}} d_{L,28}^{-2}.
\end{aligned} \tag{4}$$

Regime V:

$$\begin{aligned}
r_{\text{ra}} &= 2.15 \times 10^{10} \text{ cm } r_{0,9} \eta_2^{1/3} (1 + \sigma_0)_2^{1/3}, \\
r_c &= 1.0 \times 10^{\frac{31\delta+8}{3\delta}} \text{ cm } r_{0,9} \eta_2^{\frac{\delta+2}{3\delta}} (1 + \sigma_0)_2^{\frac{\delta+2}{3\delta}}, \\
r_{\text{ph}} &= 5.8 \times 10^{\frac{62\delta+34}{6\delta+3}} \text{ cm } L_{w,52}^{\frac{1}{2\delta+1}} r_{0,9}^{\frac{2\delta}{2\delta+1}} \eta_2^{\frac{2\delta-5}{6\delta+3}} (1 + \sigma_0)_2^{\frac{2\delta-5}{6\delta+3}}, \\
\Gamma_{\text{ph}} &= 5.8 \times 10^{\frac{11\delta+4}{6\delta+3}} L_{w,52}^{\frac{\delta}{2\delta+1}} r_{0,9}^{-\frac{\delta}{2\delta+1}} \eta_2^{\frac{1-4\delta}{6\delta+3}} (1 + \sigma_0)_2^{\frac{1-4\delta}{6\delta+3}}, \\
1 + \sigma_{\text{ph}} &= 10^{\frac{19\delta+2}{2\delta+1}} e^{-\frac{43.2\delta}{2\delta+1}} L_{w,52}^{-\frac{\delta}{2\delta+1}} r_{0,9}^{\frac{\delta}{2\delta+1}} \eta_2^{\frac{10\delta+2}{6\delta+3}} (1 + \sigma_0)_2^{\frac{10\delta+2}{6\delta+3}}, \\
kT_{\text{BB}}^{\text{eff}} &= 8.2 \times 10^{\frac{112-133\delta}{24\delta+12}} e^{\frac{129.6\delta-86.4}{8\delta+4}} \text{ keV } (1+z)^{-1} L_{w,52}^{\frac{5\delta-1}{8\delta+4}} r_{0,9}^{-\frac{7\delta}{8\delta+4}} \eta_2^{\frac{2-3\delta}{4\delta+2}} (1 + \sigma_0)_2^{\frac{3-8\delta}{8\delta+4}}, \\
F_{\text{ph}} &= 5.8 \times 10^{-\frac{13\delta+7}{2\delta+1}} \text{ erg s}^{-1} \text{ cm}^{-2} L_{w,52}^{\frac{3\delta+1}{2\delta+1}} r_{0,9}^{-\frac{\delta}{2\delta+1}} \eta_2^{-\frac{2\delta}{2\delta+1}} (1 + \sigma_0)_2^{-\frac{4\delta+1}{2\delta+1}} d_{L,28}^{-2}.
\end{aligned} \tag{5}$$

Regime VI:

$$\begin{aligned}
r_{\text{ra}} &= 2.15 \times 10^{10} \text{ cm } r_{0,9} \eta_2^{1/3} (1 + \sigma_0)_2^{1/3}, \\
r_{\text{c}} &= 1.0 \times 10^{\frac{31\delta+8}{3\delta}} \text{ cm } r_{0,9} \eta_2^{\frac{\delta+2}{3\delta}} (1 + \sigma_0)_2^{\frac{\delta+2}{3\delta}}, \\
r_{\text{ph}} &= 5.81 \times 10^{12} \text{ cm } L_{w,52} \eta_1^{-3} (1 + \sigma_0)_1^{-3}, \\
1 + \Gamma_{\text{ph}} &= 100 \eta_1 (1 + \sigma_0)_1, \\
1 + \sigma_{\text{ph}} &\simeq 1, \\
kT_{\text{BB}}^{\text{eff}} &= 8.6 \times 10^{\frac{2}{9\delta}} \text{ keV } (1 + z)^{-1} L_{w,52}^{-5/12} r_{0,9}^{1/6} \eta_1^{\frac{49\delta+2}{18\delta}} (1 + \sigma_0)_1^{\frac{89\delta+4}{36\delta}}, \\
F_{\text{ph}} &= 2.0 \times 10^{\frac{8-63\delta}{9\delta}} \text{ erg s}^{-1} \text{cm}^{-2} L_{w,52}^{1/3} r_{0,9}^{2/3} \eta_1^{\frac{26\delta+4}{9\delta}} (1 + \sigma_0)_1^{\frac{17\delta+4}{9\delta}} d_{L,28}^{-2}.
\end{aligned} \tag{6}$$

For the general δ models, the criteria of all the twelve regimes based on the central engine properties are collected in Table 3.

	$r_{\text{ph}} < r_{\text{ra}}$	$r_{\text{ra}} < r_{\text{ph}} < r_{\text{c}}$	$r_{\text{ph}} > r_{\text{c}}$
Non-dissipation	Regime I	Regime II	Regime III
$\eta > (1 + \sigma_0)^{1/2}$	$\eta^{12/5}(1 + \sigma_0)^{3/5} > 7.22 \times 10^5 L_{w,52}^{3/5} r_{0,9}^{-3/5}$	$\eta^{12/5}(1 + \sigma_0)^{3/5} < 7.22 \times 10^5 L_{w,52}^{3/5} r_{0,9}^{-3/5}$ $\eta^{12/5}(1 + \sigma_0)^{18/5} > 7.22 \times 10^5 L_{w,52}^{3/5} r_{0,9}^{-3/5}$	$\eta^{12/5}(1 + \sigma_0)^{18/5} < 7.22 \times 10^5 L_{w,52}^{3/5} r_{0,9}^{-3/5}$
Non-dissipation	Regime IV	Regime V	Regime VI
$\eta < (1 + \sigma_0)^{1/2}$	$\eta^{6/5}(1 + \sigma_0)^{6/5} > 7.22 \times 10^5 L_{w,52}^{3/5} r_{0,9}^{-3/5}$	$\eta^{6/5}(1 + \sigma_0)^{6/5} < 7.22 \times 10^5 L_{w,52}^{3/5} r_{0,9}^{-3/5}$ $\eta^{16/5}(1 + \sigma_0)^{16/5} > 7.22 \times 10^5 L_{w,52}^{3/5} r_{0,9}^{-3/5}$	$\eta^{16/5}(1 + \sigma_0)^{16/5} < 7.22 \times 10^5 L_{w,52}^{3/5} r_{0,9}^{-3/5}$
Dissipation	Regime I	Regime II	Regime III
$\eta > (1 + \sigma_0)^{1/2}$	$\eta^{12/5}(1 + \sigma_0)^{3/5} > 7.22 \times 10^5 L_{w,52}^{3/5} r_{0,9}^{-3/5}$	$\eta^{12/5}(1 + \sigma_0)^{3/5} < 7.22 \times 10^5 L_{w,52}^{3/5} r_{0,9}^{-3/5}$ $\eta^{12/5}(1 + \sigma_0)^{18/5} > 7.22 \times 10^5 L_{w,52}^{3/5} r_{0,9}^{-3/5}$	$\eta^{12/5}(1 + \sigma_0)^{18/5} < 7.22 \times 10^5 L_{w,52}^{3/5} r_{0,9}^{-3/5}$
Dissipation	Regime IV	Regime V	Regime VI
$\eta < (1 + \sigma_0)^{1/2}$	$\eta^{6/5}(1 + \sigma_0)^{6/5} > 7.22 \times 10^5 L_{w,52}^{3/5} r_{0,9}^{-3/5}$	$\eta^{6/5}(1 + \sigma_0)^{6/5} < 7.22 \times 10^5 L_{w,52}^{3/5} r_{0,9}^{-3/5}$ $\eta^{16/5}(1 + \sigma_0)^{16/5} > 7.22 \times 10^5 L_{w,52}^{3/5} r_{0,9}^{-3/5}$	$\eta^{16/5}(1 + \sigma_0)^{16/5} < 7.22 \times 10^5 L_{w,52}^{3/5} r_{0,9}^{-3/5}$

Table 1: Definition and theoretical criteria of r_{ph} regimes for different models, with $\delta = 1/3$.

No dissipation Regime II	
$14.8(1+z)^{1/4}(\frac{kT_{\text{ob}}}{50 \text{ keV}})^{1/4}(\frac{F_{\text{BB}}}{10^{-8} \text{ erg s}^{-1} \text{ cm}^{-2}})^{3/16}r_{0,9}^{-1/8}f_{\text{th},-1}^{1/2}f_{\gamma}^{1/2}d_{L,28}^{3/8} > 1$	
$0.24(1+z)^{-3}(\frac{kT_{\text{ob}}}{50 \text{ keV}})^{-3}(\frac{F_{\text{BB}}}{10^{-8} \text{ erg s}^{-1} \text{ cm}^{-2}})^{3/4}r_{0,9}^{-3/2}d_{L,28}^{3/2} > 1$	
$1.43 \times 10^{-5}(1+z)^{-7}(\frac{kT_{\text{ob}}}{50 \text{ keV}})^{-7}(\frac{F_{\text{BB}}}{10^{-8} \text{ erg s}^{-1} \text{ cm}^{-2}})^{7/4}r_{0,9}^{-7/2}f_{\text{th},-1}^3f_{\gamma}^3d_{L,28}^{7/2} < 1$	
No dissipation Regime III	
$8.28(1+z)^{-3/2}(\frac{kT_{\text{ob}}}{30 \text{ keV}})^{-3/2}(\frac{F_{\text{BB}}}{10^{-7} \text{ erg s}^{-1} \text{ cm}^{-2}})^{5/8}r_{0,9}^{-1}f_{\text{th},-1}^{5/4}f_{\gamma}^{5/4}d_{L,28}^{5/4} > 1$	
$9.42 \times 10^{-2}(1+z)^{-14/3}(\frac{kT_{\text{ob}}}{30 \text{ keV}})^{-14/3}(\frac{F_{\text{BB}}}{10^{-7} \text{ erg s}^{-1} \text{ cm}^{-2}})^{7/6}r_{0,9}^{-7/3}f_{\text{th},-1}^2f_{\gamma}^2d_{L,28}^{7/3} > 1$	
Non-dissipation Regime V	
$41.4(1+z)^{1/2}(\frac{kT_{\text{ob}}}{10 \text{ keV}})^{1/2}(\frac{F_{\text{BB}}}{10^{-9} \text{ erg s}^{-1} \text{ cm}^{-2}})^{3/8}r_{0,9}^{-1/4}f_{\text{th},-1}f_{\gamma}d_{L,28}^{3/4} < 1$	
$5.28(1+z)^{-3}(\frac{kT_{\text{ob}}}{10 \text{ keV}})^{-3}(\frac{F_{\text{BB}}}{10^{-9} \text{ erg s}^{-1} \text{ cm}^{-2}})^{3/4}r_{0,9}^{-3/2}d_{L,28}^{3/2} > 1$	
$1.16 \times 10^{-5}(1+z)^{-8}(\frac{kT_{\text{ob}}}{10 \text{ keV}})^{-8}(\frac{F_{\text{BB}}}{10^{-9} \text{ erg s}^{-1} \text{ cm}^{-2}})r_{0,9}^{-3}f_{\text{th},-1}f_{\gamma}d_{L,28}^2 < 1$	
Non-dissipation Regime VI	
$8.28(1+z)^{-3/2}(\frac{kT_{\text{ob}}}{30 \text{ keV}})^{-3/2}(\frac{F_{\text{BB}}}{10^{-7} \text{ erg s}^{-1} \text{ cm}^{-2}})^{5/8}r_{0,9}^{-1}f_{\text{th},-1}^{5/4}f_{\gamma}^{5/4}d_{L,28}^{5/4} < 1$	
$5.63 \times 10^{-3}(1+z)^{-8/3}(\frac{kT_{\text{ob}}}{30 \text{ keV}})^{-8/3}(\frac{F_{\text{BB}}}{10^{-7} \text{ erg s}^{-1} \text{ cm}^{-2}})^{1/3}r_{0,9}^{-1}f_{\text{th},-1}^{1/3}f_{\gamma}^{1/3}d_{L,28}^{2/3} > 1$	

Table 2: Observational criteria of r_{ph} regimes for different models.

	$r_{\text{ph}} < r_{\text{ra}}$	$r_{\text{ra}} < r_{\text{ph}} < r_{\text{c}}$	$r_{\text{ph}} > r_{\text{c}}$
Non-dissipation	Regime I	Regime II	Regime III
$\eta^{12/5}(1+\sigma_0)^{3/5} > 7.22 \times 10^5 L_{w,52}^{3/5} r_{0,9}^{-3/5}$		$\eta^{\frac{4}{2\delta+1}}(1+\sigma_0)^{\frac{1}{2\delta+1}} < 5.81 \times 10^{\frac{9}{2\delta+1}} L_{w,52}^{\frac{1}{2\delta+1}} r_{0,9}^{-\frac{1}{2\delta+1}}$	$\eta^{12/5}(1+\sigma_0)^{\frac{9\delta+3}{5\delta}} < 7.22 \times 10^5 L_{w,52}^{3/5} r_{0,9}^{-3/5}$
$\eta > (1+\sigma_0)^{1/2}$		$\eta^{\frac{4}{2\delta+1}}(1+\sigma_0)^{\frac{3\delta+1}{\delta(2\delta+1)}} > 5.81 \times 10^{\frac{9}{2\delta+1}} L_{w,52}^{\frac{1}{2\delta+1}} r_{0,9}^{-\frac{1}{2\delta+1}}$	
Non-dissipation	Regime IV	Regime V	Regime VI
$\eta^{6/5}(1+\sigma_0)^{6/5} > 7.22 \times 10^5 L_{w,52}^{3/5} r_{0,9}^{-3/5}$		$\eta^{\frac{2}{2\delta+1}}(1+\sigma_0)^{\frac{2}{2\delta+1}} < 5.81 \times 10^{\frac{9}{2\delta+1}} L_{w,52}^{\frac{1}{2\delta+1}} r_{0,9}^{-\frac{1}{2\delta+1}}$	$\eta^{\frac{10\delta+2}{5\delta}}(1+\sigma_0)^{\frac{10\delta+2}{5\delta}} < 7.22 \times 10^5 L_{w,52}^{3/5} r_{0,9}^{-3/5}$
$\eta < (1+\sigma_0)^{1/2}$		$\eta^{\frac{10\delta+2}{3\delta(2\delta+1)}}(1+\sigma_0)^{\frac{10\delta+2}{3\delta(2\delta+1)}} > 5.81 \times 10^{\frac{9}{2\delta+1}} L_{w,52}^{\frac{1}{2\delta+1}} r_{0,9}^{-\frac{1}{2\delta+1}}$	
Dissipation	Regime I	Regime II	Regime III
$\eta^{12/5}(1+\sigma_0)^{3/5} > 7.22 \times 10^5 L_{w,52}^{3/5} r_{0,9}^{-3/5}$		$\eta^{\frac{4}{2\delta+1}}(1+\sigma_0)^{\frac{1}{2\delta+1}} < 5.81 \times 10^{\frac{9}{2\delta+1}} L_{w,52}^{\frac{1}{2\delta+1}} r_{0,9}^{-\frac{1}{2\delta+1}}$	$\eta^{12/5}(1+\sigma_0)^{\frac{9\delta+3}{5\delta}} < 7.22 \times 10^5 L_{w,52}^{3/5} r_{0,9}^{-3/5}$
$\eta > (1+\sigma_0)^{1/2}$		$\eta^{\frac{4}{2\delta+1}}(1+\sigma_0)^{\frac{3\delta+1}{\delta(2\delta+1)}} > 5.81 \times 10^{\frac{9}{2\delta+1}} L_{w,52}^{\frac{1}{2\delta+1}} r_{0,9}^{-\frac{1}{2\delta+1}}$	
Dissipation	Regime IV	Regime V	Regime VI
$\eta^{6/5}(1+\sigma_0)^{6/5} > 7.22 \times 10^5 L_{w,52}^{3/5} r_{0,9}^{-3/5}$		$\eta^{\frac{2}{2\delta+1}}(1+\sigma_0)^{\frac{2}{2\delta+1}} < 5.81 \times 10^{\frac{9}{2\delta+1}} L_{w,52}^{\frac{1}{2\delta+1}} r_{0,9}^{-\frac{1}{2\delta+1}}$	$\eta^{\frac{10\delta+2}{5\delta}}(1+\sigma_0)^{\frac{10\delta+2}{5\delta}} < 7.22 \times 10^5 L_{w,52}^{3/5} r_{0,9}^{-3/5}$
$\eta < (1+\sigma_0)^{1/2}$		$\eta^{\frac{10\delta+2}{3\delta(2\delta+1)}}(1+\sigma_0)^{\frac{10\delta+2}{3\delta(2\delta+1)}} > 5.81 \times 10^{\frac{9}{2\delta+1}} L_{w,52}^{\frac{1}{2\delta+1}} r_{0,9}^{-\frac{1}{2\delta+1}}$	

Table 3: Definition and theoretical criteria of r_{ph} regimes for different models, with general δ value.

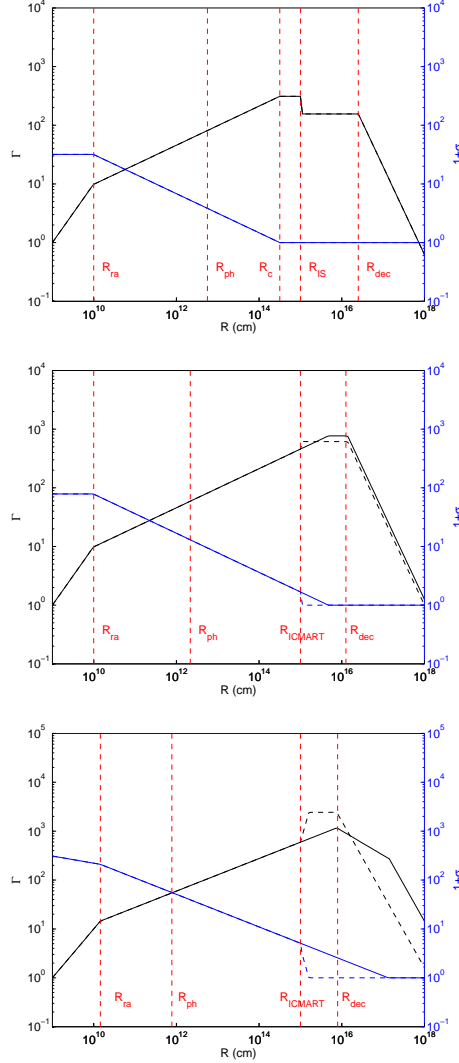


Fig. 1.— Examples of GRB jet dynamics. Black lines are for Γ evolution and blue lines are for σ evolution. Vertical dashed lines denote some characteristic radii: rapid acceleration radius r_{ra} , photosphere radius r_{ph} , coasting radius r_c , internal shock radius r_{IS} , ICMART radius r_{ICMART} , and deceleration radius r_{dec} . Following parameters are adopted: $L_w = 10^{52} \text{ erg s}^{-1}$, and $r_0 = 10^9 \text{ cm}$. Different panels correspond to different combinations of η and σ_0 . Top panel: $\eta = 10$ and $\sigma_0 = 30$. Internal shocks can form, which dissipate energy and reduce the total kinetic energy in the system; Middle panel: $\eta = 10$ and $\sigma_0 = 80$; Bottom panel, $\eta = 10$ and $\sigma_0 = 300$. In both cases, σ is above unity at 10^{15} cm , suggesting that ICMART events may be the main mechanism to dissipate magnetic energy and power non-thermal radiation. The dashed lines denote the consequences of ICMART events: an abrupt reduction of σ and a sudden acceleration of the system (Zhang & Yan 2011).

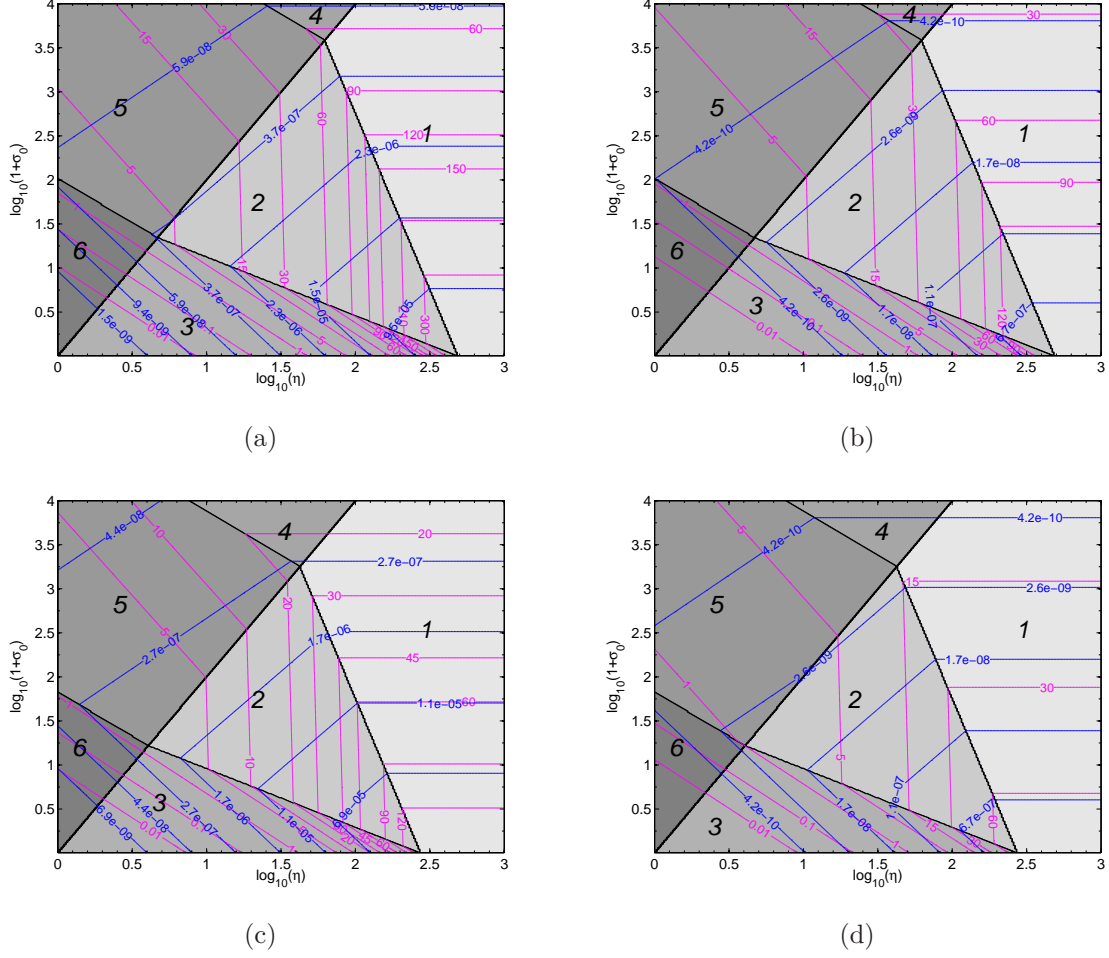


Fig. 2.— Contour plots of T_{ob} and F_{BB} in the $(\eta, 1 + \sigma)$ domain in the non-dissipative photosphere scenario. Pink lines are for T_{ob} in units of keV, and blue lines are for F_{BB} in units of $\text{erg cm}^{-2} \text{s}^{-1}$. The six regimes for the photosphere radius are shown in different grey blocks, with higher regime number ones marked with darker grey and the regime number marked in the block. For all the examples, $L_w = 10^{52} \text{erg s}^{-1}$ is assumed. Top (bottom) panels are for $r_0 = 10^8 \text{cm}$ ($r_0 = 10^9 \text{cm}$), respectively; and left (right) panels are for $z = 0.1$ ($z = 1$), respectively.

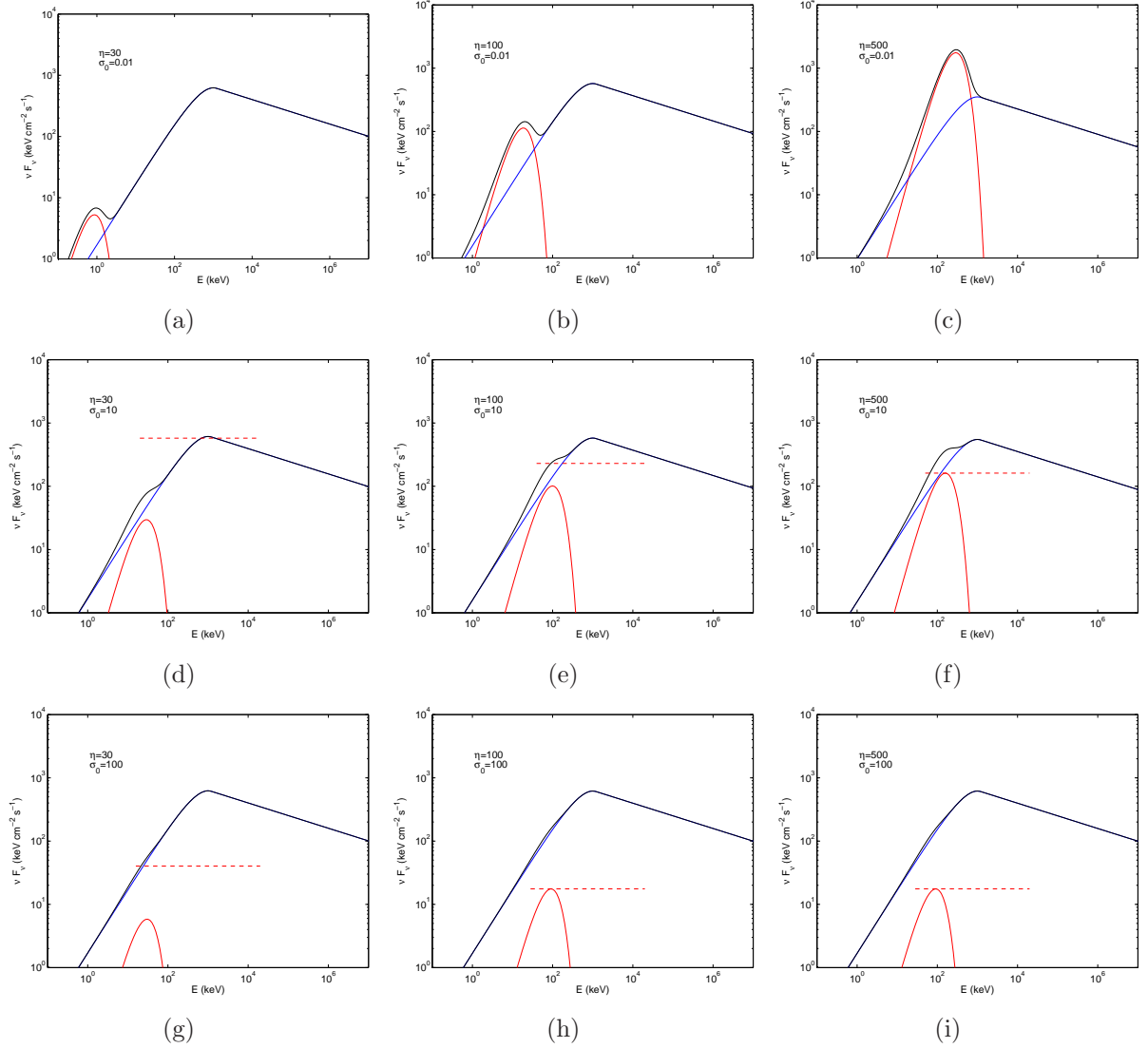


Fig. 3.— Example model spectra of GRB prompt emission. Red, blue and black lines are for the thermal (non-dissipative photosphere scenario), non-thermal, and total spectral components, respectively. Here we adopt $L_w = 10^{52} \text{erg s}^{-1}$, $r_0 = 10^9 \text{cm}$, and $z = 1$. Different panels correspond to different combination of η and σ_0 (as marked in the inset of each panel). The non-thermal radiation efficiency is assumed as 50%, and a typical Band function shape is adopted. Dashed lines represent the flux and E_p range of photosphere emission for the dissipative photosphere scenario. The lower limit of E_p is calculated assuming the photosphere emission is thermal, and the upper limit is fixed as 20 Mev (Beloborodov 2013).

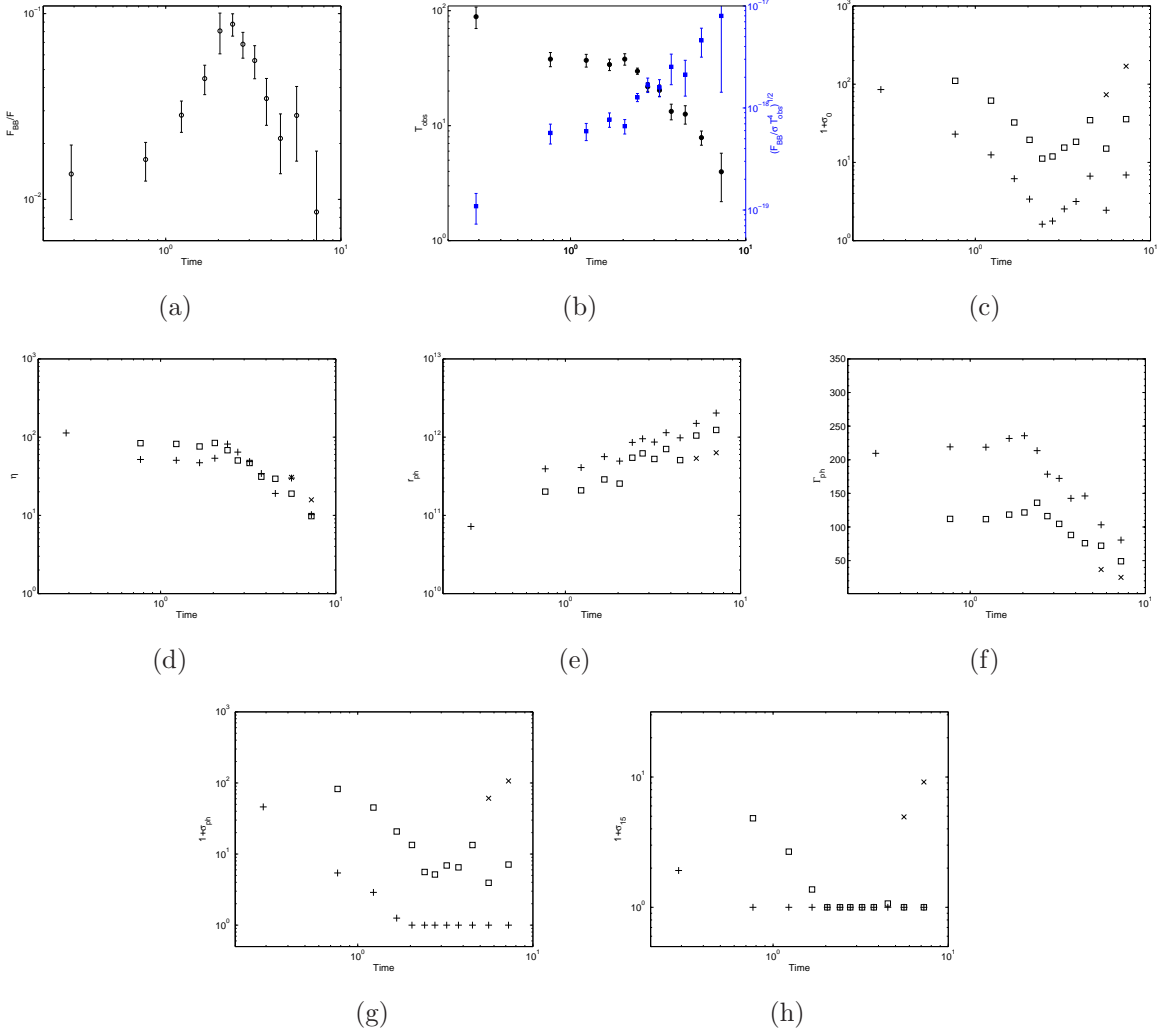


Fig. 4.— A case study for GRB 110721A. The observed $F_{\text{BB}}/F_{\text{ob}}$ (a) and the observed T_{BB} and $(F_{\text{BB}}/\sigma T_{\text{ob}}^4)^{1/2}$ (b) evolution (Iyyani et al. 2013), along with the derived parameters of a non-dissipative photosphere and their evolution: $1 + \sigma_0$ (c), η (d), r_{ph} (e), Γ_{ph} (f), $(1 + \sigma_{\text{ph}})$ (g), and $(1 + \sigma_{15})$ (h). The plus, square and cross symbols denote the cases with $r_0 = 10^8$ cm, 10^9 cm and 10^{10} cm, respectively.

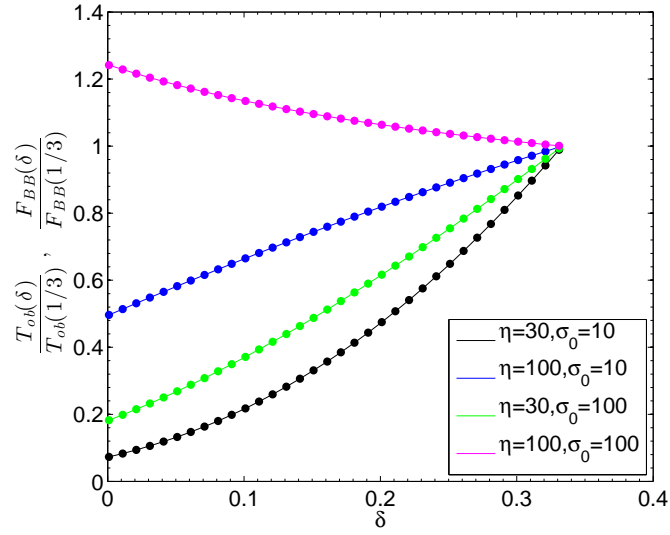


Fig. 5.— Variation of $\frac{T_{ob}(\delta)}{T_{ob}(1/3)}$ (solid lines) and $\frac{F_{BB}(\delta)}{F_{BB}(1/3)}$ (dotted lines) as a function of δ in the non-dissipative photosphere models.